Science and Technology Facilities Council

Technical Report
STFC-TR-2024-005

Technical design document for the LMX diffractometer
Version 2.2

N Funnell, S Capelli, M Gutmann,
P Henry, S Hull, D Keen, M Ritchie,
C Bull

November 2024

Enquiries concerning this report should be addressed to:

RAL Library
STFC Rutherford Appleton Laboratory
Harwell Oxford
Didcot
OX11 0QX

Tel: +44(0)1235 445577
email: library@stfc.ac.uk

Science and Technology Facilities Council reports are available online at: https://epubs.stfc.ac.uk

Accessibility: a Microsoft Word version of this document (for use with assistive technology) may be available on request.

DOI: 10.5286/stfctr.2024005

ISSN 2753-5797

STFC Author Identifiers (ORCIDs)

Author ORCIDs are provided where available.

Nicholas Funnell	[0000-0001-6280-036X](https://orcid.org/0000-0001-6280-036X)
Silvia Capelli	[0000-0001-8765-7432](https://orcid.org/0000-0001-8765-7432)
Paul Henry	[0000-0003-4714-6587](https://orcid.org/0000-0003-4714-6587)
David Keen	[0000-0003-0376-2767](https://orcid.org/0000-0003-0376-2767)
Craig Bull	[0000-0002-5170-6674](https://orcid.org/0000-0002-5170-6674)

Technical design document for the LMX diffractometer

Version 2.2

– revised to address recommendations from internal review and additional post-review comments —

Table of Contents

1) Project title and the scientific design team

LMX – Large molecule, single-crystal diffractometer

Nicholas Funnell, Silvia Capelli, Matthias Gutmann, Paul Henry, Stephen Hull, David Keen, Michael Ritchie, and Craig Bull.

2) Project description

LMX is an instrument dedicated to the measurement of large-molecule structures by single-crystal diffraction. This will enable the crystallographic characterisation of biological macromolecules and topical ‘chemical’ crystal structures, including supramolecular materials, frameworks and large pharmaceuticals. The instrument will provide brand new science capability for the ISIS Neutron and Muon Facility. A more substantive justification for the scientific and business cases are available in a separate document.

The instrument will measure diffraction patterns from small (≤ 1 mm^3) samples, via a detector array with large solid angle coverage to minimise the number of crystal orientations that need to be sampled in order to measure as ‘complete’ (measuring all symmetry-inequivalent reflections) a dataset as possible. A wide wavelength band will be utilised in order to maximise the number of reflections that can be measured, simultaneously, in any given crystal orientation.

The longer primary flight path, lower (tuneable) beam divergence, longer sample–detector distance, and greater flux over longer wavelengths, than the existing SXD instrument will allow for larger unit cells to be studied. The instrument design is simple, and closely replicates that of instruments at other facilities, meaning that it presents minimal technical risk. Crucially, for ISIS, LMX will provide entirely new measurement capability and the opportunity to engage with new scientific communities.

3) Key drivers

The following key drivers were identified from the science case for the instrument:

- The ability to measure data with $d_{\min} = 2$ Å for macromolecular structures, and 1 Å for smaller ‘chemical’ materials.
- Be capable of spatially, and harmonically, resolving the ($0\ k\ 0$), ($0\ k\ 1$), ($1\ k\ 0$), and ($1\ k\ 1$) reflections, where $k = 59$–61 for a cubic unit cell with $a = 120$ Å (d-spacing ≈ 2 Å; $\Delta d/d = 0.0165$).
- Use a wide wavelength band to capture H_2 moderator peak brilliance – ca. 4 Å.
- Have high brilliance transfer across all wavelengths.
- Have maximum flux centred in the range $\lambda = 2$–3 Å.
- Transport a maximum beam size of 2.5×2.5 mm^2 to the sample position, with divergence $\pm 0.4°$ but have the ability to reduce this via jaw sets.

4) The design process

The original version of the LMX TDD was assessed by an ISIS internal review panel on 14/07/23. The full list of recommendations, and a point-by-point response to each, are provided in the Appendices. The full description of the instrument design along with details of revisions made following the internal review are described through Sections 4 and 5.

Summary of instrument design revisions:

- A longer, elliptical, guide is now proposed
- Frame overlap choppers are now single-disc and have been repositioned
- An incident slit precedes the guide entry
- The detector layout is predominantly cylindrical, comprised entirely of square panels
- The instrument will use a standard Tomkinson flange

Here, we outline in detail the rationale for some of the decisions on the instrument design, all of which are intended to meet the Key Drivers.

4.1 Moderator choice

The choice of moderator is closely tied to several of the Key Drivers and forms one of the single-most important decisions for the instrument design. An overview of moderator brilliance at ISIS is shown in Figure 4.1. Of the available options, a hydrogen moderator is selected because:

- it has high brilliance near 2–3 Å; these are known (from other facilities) to be the most useful wavelengths for measuring macromolecular structures, as well as having higher brilliance across wavelengths > 3 Å compared to other available moderators. Though a methane moderator provides a sharper line shape, the greater neutron flux offered by hydrogen is preferable for poorly-scattering biological samples; it provides superior signal-to-noise – see Section 4.3. Moreover, accurate peak shape modelling is less important for single-crystal intensity integration, than it is for powder profile refinement using the Rietveld method.
- it has the largest integrated flux across a wide 4 Å wavelength band; this will be important for measuring more weakly-scattering samples – allowing reflections to be accessed with fewer sample orientations, thus reducing measurement time.
- having high brilliance across a wide waveband makes it possible to measure reflections at the *d*-spacing limit identified in the first Key Driver. From Bragg's Law:

  $$\lambda = 2d \sin\theta$$

  The minimum measurable *d*-spacing is limited by:

  $$d_{\min} = \frac{\lambda}{2}, \quad \text{where } 2\theta = 180^\circ$$

  Therefore a $d_{\min}$ of 1 Å can be accessed using λ = 1–2 Å between 2θ = 60 and 180°. A $d_{\min}$ of 2 Å is measurable using λ = 1–4 Å between 2θ = 29 and 180°.
- it continues to have higher brilliance at longer wavelengths > 4 Å, relative to the other moderators.

There are hydrogen moderators on both ISIS Target Stations (TS1 and TS2). TS1 is preferable as its sharper time pulse provides more well-defined diffraction peak shapes – a comparison of the time structures is shown in Figure 4.1. Following refurbishment of the TS1 hydrogen moderator, it offers a substantially higher brilliance per unit time than TS2 (also shown in the Figure). Moreover, there is no available hydrogen port on Target Station 2, which precludes further development of this option. Though the ports on Target Station 1 are also occupied, a few of these instruments might be usefully redeveloped.

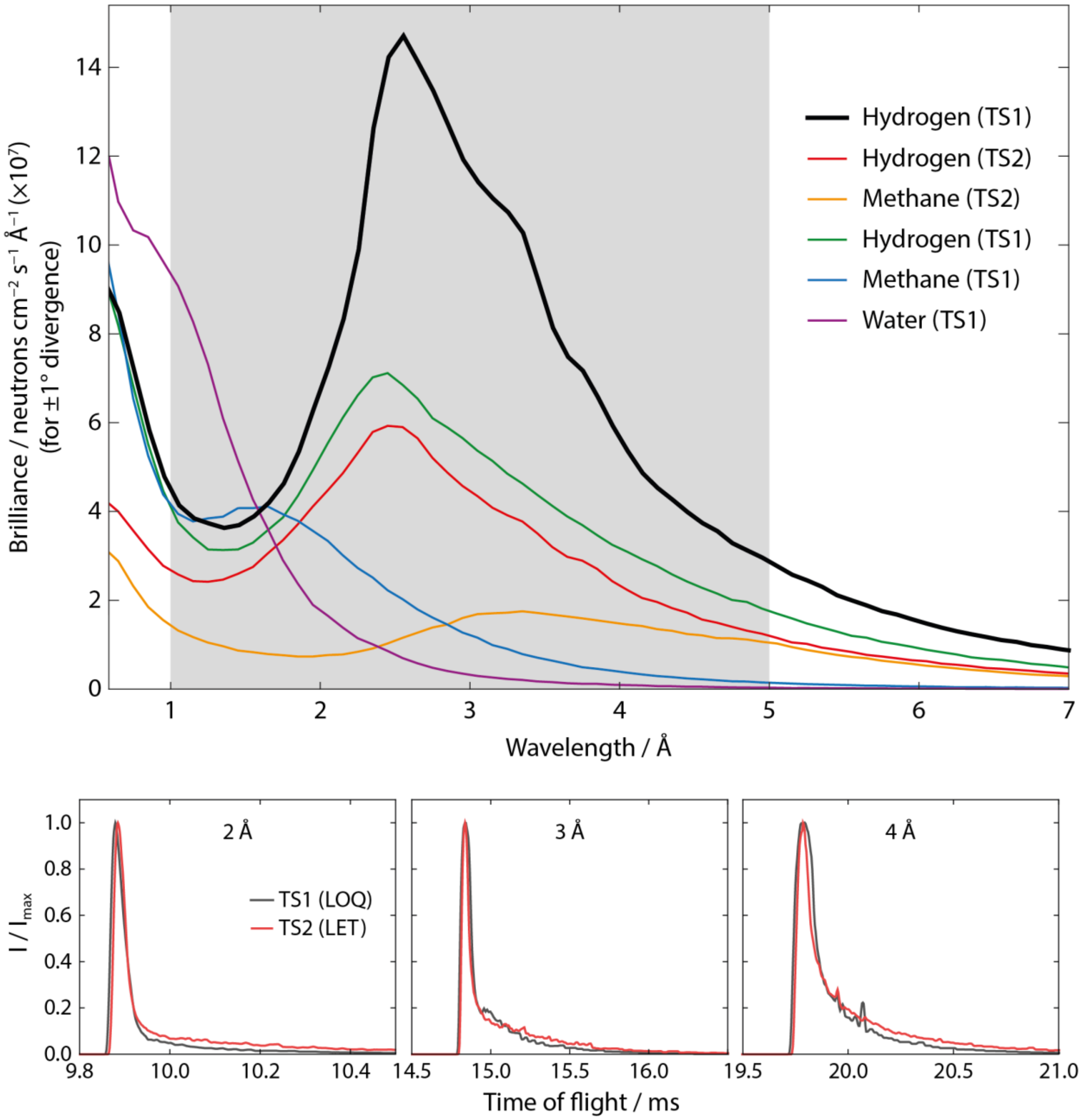

Figure 4.1. **Top:** Brilliance profiles of moderators at the ISIS Neutron and Muon Facility. The refurbished hydrogen moderator on TS1 (shown in bold, black) has the largest flux across the desired waveband for LMX, indicated by the shaded grey region. Brilliance is shown for ±1°, though relative brilliance will be invariant with divergence. **Bottom:** The time structure of (refurbished) TS1 and TS2 hydrogen moderators at L_1 = 19.5 m, each normalised to the peak maximum. Artefacts in the data are a result of simulation counting statistics.

4.2 Time-of-flight peak profiles from the hydrogen moderator

Following the refurbishment of the TS1 moderators, the hydrogen moderator has benefitted from an increase in flux. The trade-off to this is a longer peak tail (relative to the pre-refurbished moderator), which is dependent on both wavelength and scattering angle. However, in this section, it will be shown that this does not present a problem for data processing on LMX. Figure 4.2 shows a comparison of the time structures between the old, and new, hydrogen moderators as viewed by the LOQ instrument, for λ = 2 and 4 Å.

Single-crystal measurements do not typically require highly-accurate peak fitting in order to extract intensities, in contrast to analysis of powder data by Rietveld refinement which uses point-by-point fitting. However, it is still advantageous to fit these as accurately as possible, to better resolve overlapped peaks, as well as determining how many time channels to integrate over. It is worth noting that the proportion of measurable reflections that coincide spatially (i.e. harmonic reflections) is very small. This has been shown to be only 17% of all reflections when measuring across a 3 Å wavelength range – Cruickshank, Helliwell and Moffat, *Acta Crystallogr*. (1987), **A43**, 656–674. Therefore the overall proportion of reflections that are overlapped in both space and time is likely to be very small.

In order to fit the peaks, they are described with a sum of back-to-back exponentials, each convolved with a Gaussian function. A preliminary fit to a single diffraction peak as a function of time-of-flight (or wavelength) revealed that the individual parameters comprising the overall fit can each be approximated with empirical functions, as well as the relative peak positions, thus constraining their values. Plots of these are shown in the Appendices. Figure 4.3 shows fits to three diffraction peaks with λ = 2.1, 3.3, and 4.2 Å, at a scattering angle of 2θ = 142.5°, where only the intensity and position of the principal peak are allowed to refine.

In all cases shown, the peak shapes from the simulated data can be described using these highly-constrained functions. An example is presented in Figure 4.4 where an intense peak (‘1’) partially obscures two weaker peaks (‘2’ and ‘3’) with a long tail. By constraining the fit to only consider position and intensity parameters, the first peak can be adequately fitted and, following subtraction, the

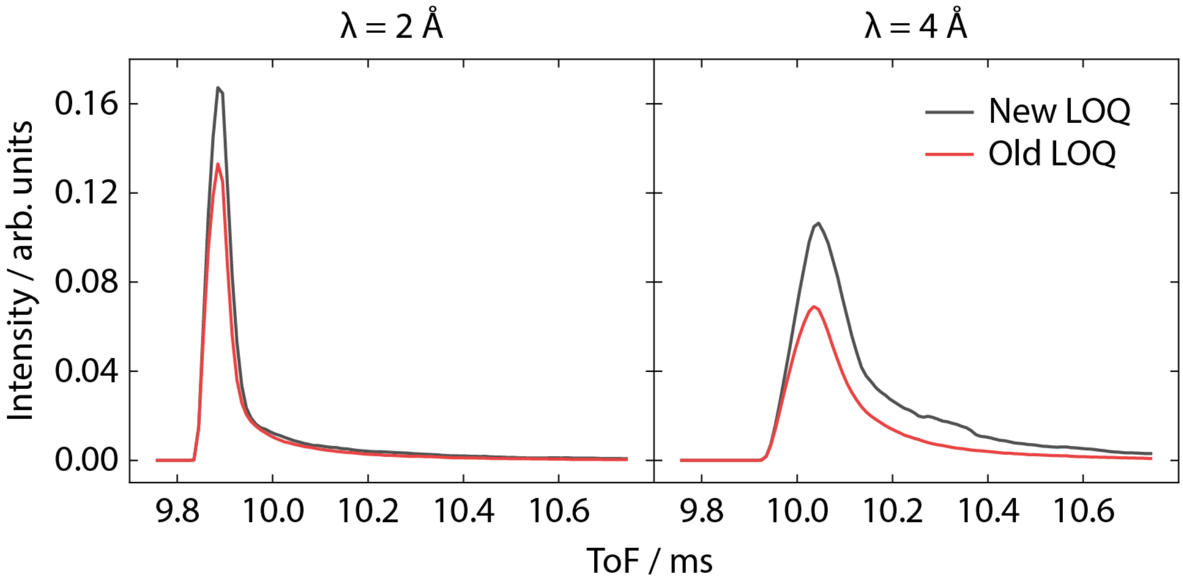

Figure 4.2. Comparison of the time structures of the old and new TS1 hydrogen moderator, centred on λ = 2 and 4 Å, without beam transport at the LOQ (N5) port.

second and third peaks can also be straightforwardly fitted. There is only a small intensity mismatch to each of the three peaks (+1.2%, −3.2%, −3.5%, respectively) when fitted as an overlapped series, versus simulating and fitting them in isolation.

Furthermore, a prerequisite to a neutron experiment is prior characterisation of the sample by X-ray diffraction, hence the unit cell will already be known as will the positions of its diffraction peaks (or at least approximately so in the case of variable-temperature experiments).

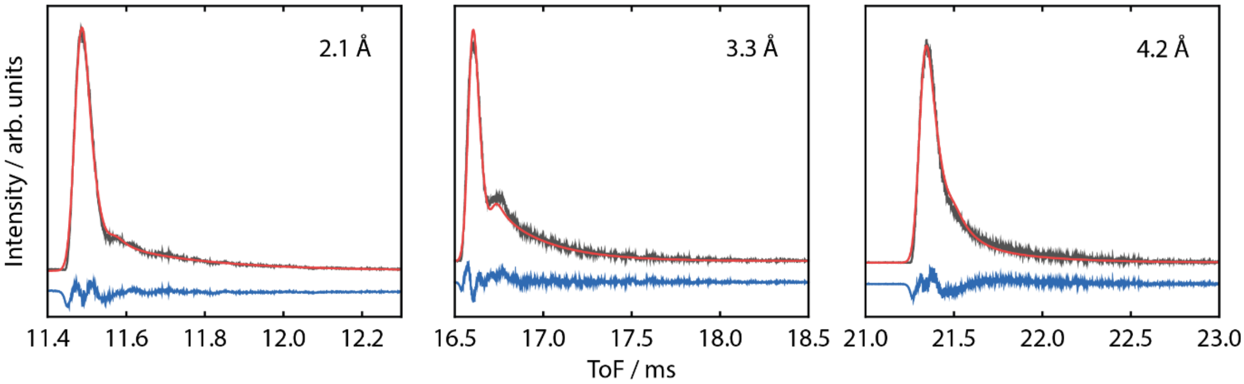

Figure 4.3. Diffraction peak fits at 2.1, 3.3, and 4.2 Å (2θ = 142.5°). Simulated data are shown in grey, the fit in red, and the difference in blue. Each fit comprises two peak contributions, where the only refined parameters are the principal peak position and intensity. All other parameters are constrained to follow pre-determined trends, shown in the Appendices.

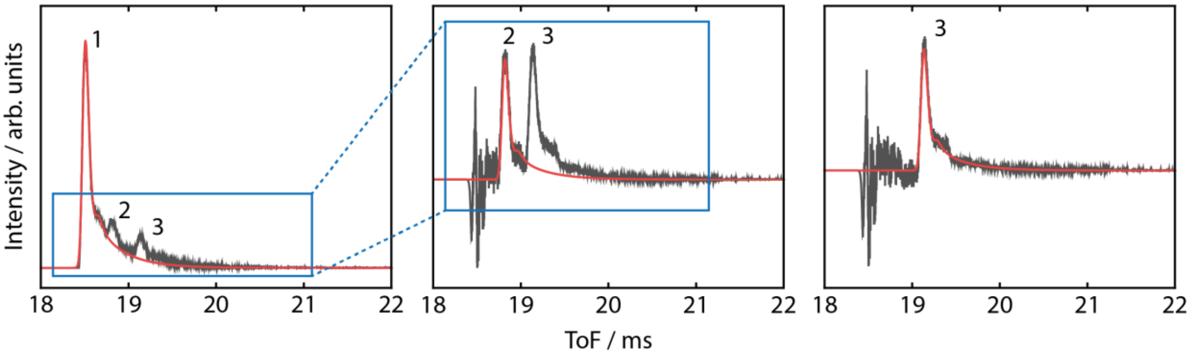

Figure 4.4. Left: Three overlapping peaks (numbered 1–3), where the first is significantly more intense than the others. After fitting the first peak, and subtracting it, the second peak can be fitted (**centre**), and then the third (**right**).

4.3 Comparison of hydrogen and methane moderator performance

One point raised during internal review was the possibility that the solid CH_4 moderator on TS2 might outperform TS1 H_2 due the favourable peak brightness of the former as opposed to the higher average brightness of the latter. Crystalline samples on LMX will typically be weakly-scattering, and it will be important to be able to distinguish weak peaks over background. Simulations were performed to assess the relative performance of the two moderators; a summary of these is shown in Figure 4.5, and is explained as follows:

Panel a). A direct comparison of the relative brilliance of the two moderators; the simulation was performed by placing a wavelength monitor at the sample position and swapping H_2 (TS1) and CH_4 (TS2) moderator components in McStas. The simulations do not account for any difference in source repetition rate; they are both normalised to 1 μA of beam current. This would otherwise favour TS1 H_2 as this is a factor of 4 higher than for TS2.

Panel b). A ratio of the brilliance plots shown in panel **a)**. H_2 has a higher (average) brilliance between ca. 2–4 Å and at $\lambda > 6$ Å.

Panel c). A series of powder peaks at $2\theta = 30°$ (where diffraction peaks are inherently broader cf. backscattering), simulated as a function of wavelength and H_2/CH_4 moderators. The *d*-spacing of each peak is varied to fulfil the Bragg condition, given the scattering angle and wavelength. These simulations represent an 'infinitely-long' counting time – perfect signal-to-noise statistics in the case of both moderators. It therefore follows that the relative integrated fluxes of the H_2 and CH_4 peaks at each wavelength mirror the behaviour of the respective moderator brilliance: H_2 has higher flux between $\lambda = 2$–4 Å and at $\lambda > 6$ Å. Note that at $\lambda = 3$ Å, the CH_4 moderator produces a sharper peak, with a slightly larger intensity maximum, but the H_2 has more integrated flux overall due to its broader peak shape.

However, the most important feature of diffraction peaks is not their absolute intensity, but their clarity over background noise levels – I/σ is a more important performance metric. The key comparison that needs to be made between CH_4 and H_2 moderators is which gives better I/σ values. So far, this performance comparison has not yet considered the source repetition rates for each target station. Therefore the optimum moderator should provide better I/σ values across the majority of desired wavelength range, in the fastest measurement time.

To account for the difference in source repetition rate between the two moderators, the number of Monte-Carlo-generated neutron rays was increased for simulations using the TS1 H_2 moderator. First a 4× multiplier was applied to account for the different repetition rates of TS1 and TS2, then a subsequent wavelength-dependent scaling value (as per panel **b)**) corrected for the brilliance difference. This enabled a comparison per unit time.

Simulated background was included by using an incoherent scattering contribution – built into the 'PowderN' component in McStas. At each wavelength, the corresponding diffraction peak at $2\theta = 30°$ was assigned an arbitrary intensity. Then, across separate simulations, the value of the incoherent scattering was progressively increased until the level of simulated background scattering made identification of the peak impossible. Note that the absolute values of incoherent scattering are not meaningful, due to the diffraction peaks having arbitrary intensity. The simulated peaks and background were fitted in Topas Academic, to extract peak intensities and their associated uncertainties.

Panel d). The resulting *I*/σ values from the simulations using the process detailed above, as a function of wavelength, for both moderators.

The *I*/σ values obtained from the fits are superior for the H_2 moderator across all simulated wavelengths (1–5, 10 Å). The fitting statistics for larger incoherence values converge at ca. 0 when the peak is too weak to be identified when using either moderator. This shows that, despite the additional brilliance that the CH_4 moderator provides at select wavelengths, as well as its sharper time structure, the repetition rate of TS1 is the more important factor; the H_2 moderator provides superior counting statistics and improved *I*/σ values.

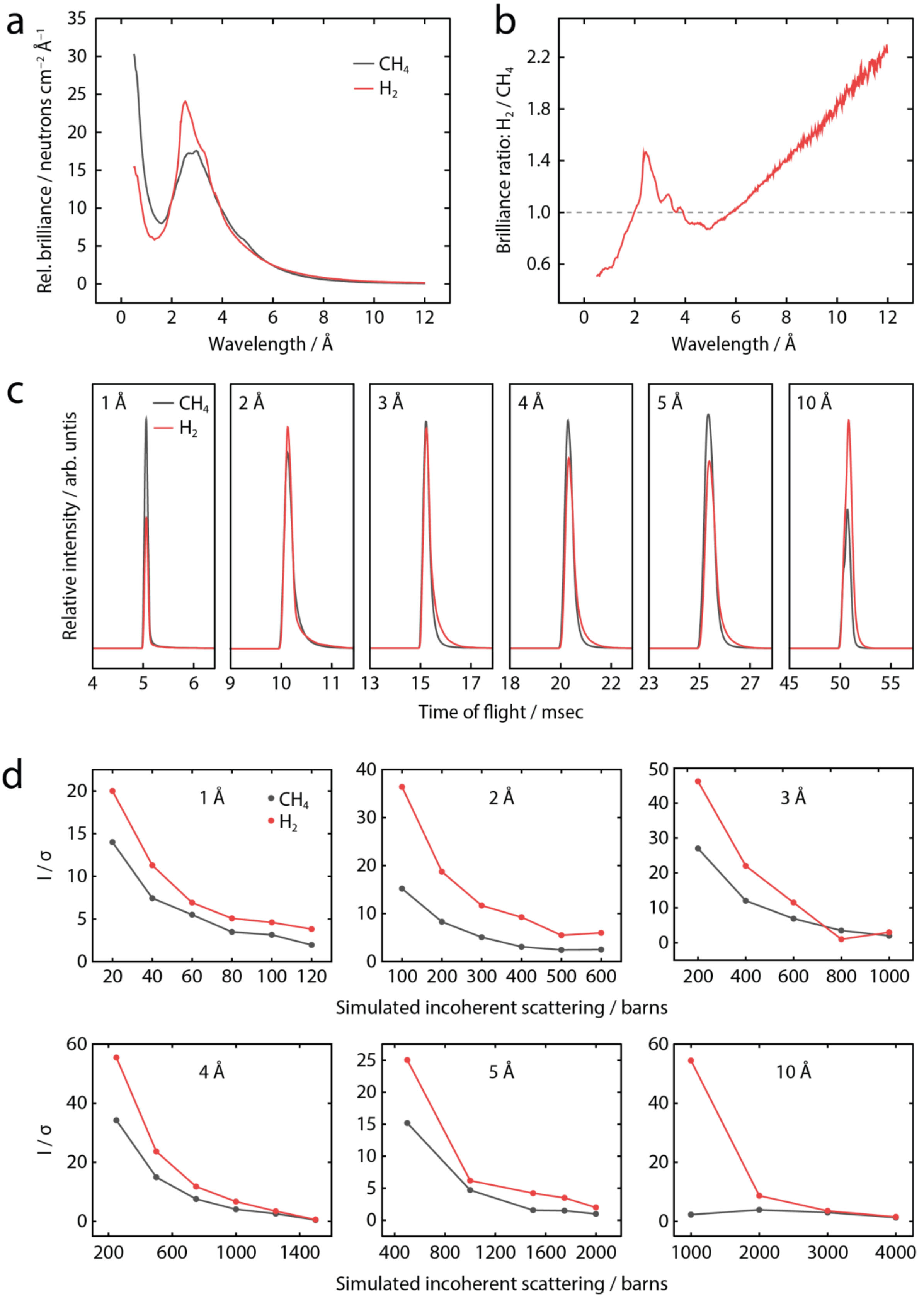

Figure 4.5. Please refer to the main text for a detailed description of this Figure. **a)** Relative brilliance between H_2 (red) and CH_4 (black) moderators, and **b)** the ratio between these. **c)** Relative intensity, and time structure of simulated diffraction peaks using the moderator brilliances in **a)**. **d)** *I*/σ values extracted from peak fitting in the presence of increasing incoherent background levels. The absolute values of incoherent scattering are not meaningful.

4.4 *Primary flight path length*

The length of the incident flight path L_1 defines both the time resolution and the wavelength range. The time resolution required was set by the Key Drivers; the ability to resolve (0 *k* 0) reflections, where *k* = 59–61, corresponding to reflections with *d*-spacing = 2.034, 2.000, and 1.967 Å, The ability to distinguish these reflections ($\Delta d/d$) is determined by the resolution function:

$$\left(\frac{\Delta d}{d}\right)^2 = \left(\frac{\Delta t}{t}\right)^2 + \left(\frac{\Delta L}{L}\right)^2 + (\cot\theta\,\Delta\theta)^2$$

The ($\Delta L/L$) contribution is negligible and $\cot\theta \rightarrow 0$ as $2\theta \rightarrow 180°$. Thus at large scattering angles $\Delta d/d \approx \Delta t/t$. For the reflection class noted above, $\Delta d/d = 0.0165$, which imposes the equivalent constraint on the LMX time structure $\Delta t/t$. Figure 4.6 shows how $\Delta t/t$ varies as a function of L_1, derived from fitting a simulated powder diffraction peak (*d* = 1.92 Å). The long tail and composite nature of the peak shape (discussed in Section 4.2) complicates determination of the peak FWHM through single peak fitting. Thus the Figure shows $\Delta t/t$ for a fit using a back-to-back exponential convolved with a Gaussian peak, as well as manual estimation directly from the simulated data.

The plot indicates that only a short instrument length (< 8 m) would be necessary to achieve $\Delta d/d = 0.0165$. However, given the long tail of the peak, and the difficulty this poses in quantifying exactly

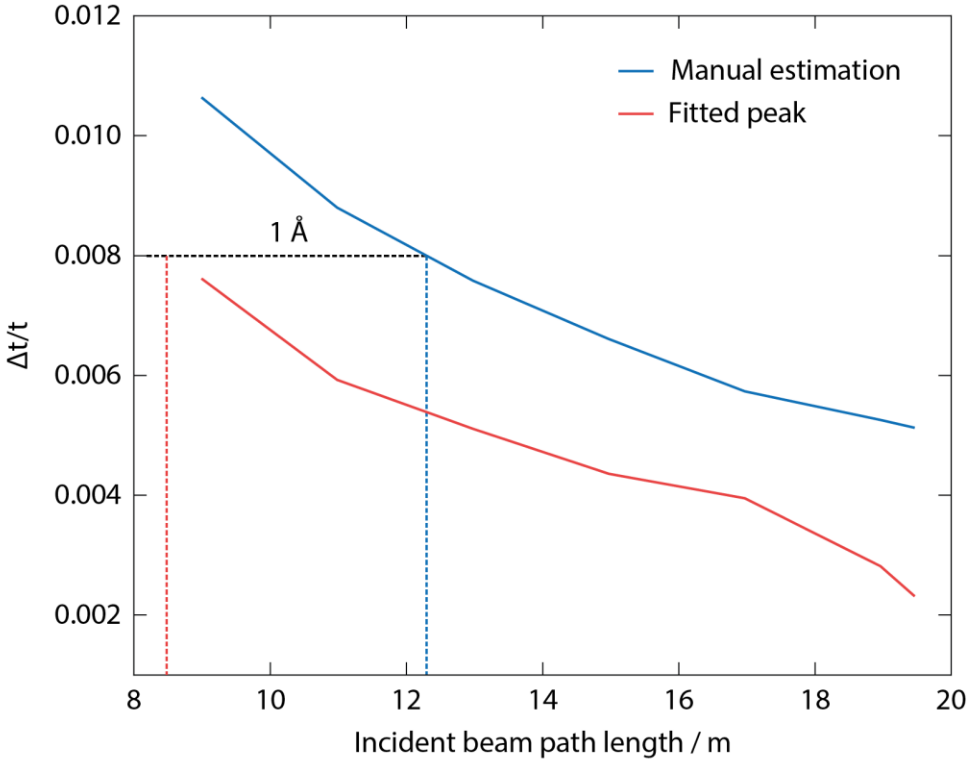

Figure 4.6. Resolution function $\Delta t/t$ relationship with incident flight path length. Two lines are shown; determination by peak fitting, and a manual estimation of the peak FWHM. In either case, for all primary path lengths simulated, the resolution of the instrument exceeds the requirements of the science drivers – to resolve 2 Å reflections of a 120 Å unit cell length ($\Delta t/t = 0.0165$). The path length required to resolve 1 Å reflections is indicated by the dotted lines.

what $\Delta d/d$ would be required (i.e. FWHM is a misleading metric for a very asymmetric peak), a longer flight path than the minimum indicated by the Figure would be prudent.

LMX also requires the ability to measure d = 1 Å reflections in chemical crystallography samples, though these are likely to consist of smaller unit cells. Nevertheless, Figure 4.5 also shows a more extreme case of $\Delta t/t$ sufficient to resolve the (0 120 0), (0 121 0) reflections (ca. 1 Å) from a 120 Å unit cell edge. A longer flight path than the minimum requirement offers flexibility for addressing complex samples in the future.

The other path length consideration is the accessible wavelength range that reaches the sample position – the maximum wavelength is given by:

$$\lambda_{\mathrm{max}} = 3956(t_{\mathrm{max}}/L_{\mathrm{tot}})$$

where t_{max} is the maximum time-of-flight (s), L_{tot} is the total flight path length (m) i.e. L_1+L_2, and t_{max} = 0.02 s (50 Hz) on TS1. A 4 Å wavelength band gives L_{tot} of 19.8 m, which in turn requires L1 ≈ 19.0–19.5 m, depending on the length of L_2. Use of frame overlap choppers with a ca. 19.5 m instrument will enable the wide 4 Å wavelength band to be tuned across a broader range of wavelengths in order to meet the requirements of a given sample being measured. At this primary flight path length, the wavelength band would span across two time frames, where prompt gamma radiation would coincide with the measurement region. This can be mitigated against by using a t_0 chopper but also by omitting select time channels if necessary (for example, the HRPD instrument at ISIS omits 170 µs across each pulse for this reason, though it does not use a t_0 chopper).

This wavelength band could still be accessed using a shorter instrument, and appropriate chopper geometry. However, the advantages in time resolution provided by a longer instrument will also apply to background signal, as well as sample scattering. Finer time binning of the background signal will be helpful in processing its removal, leading to improved signal-to-noise. The effect of using a shorter instrument (L_1 = 16 m) on time resolution, placing the wavelength band entirely within a single measurement frame is shown in the Appendix.

4.5 Sample–detector distance and pixel size

When surrounding the sample position with detectors – aiming to achieve near-4π steradian solid-angle coverage – the main limiting factor is cost. A larger L_2 allows a detector array to more closely tile a sphere, but requires more detectors at significant expense. The cheaper option of a shorter L_2 places constraints on physical space for sample environment, and also requires a much smaller pixel size (also with cost implications) to maintain a given spatial resolution.

The starting point for L_2 was 0.5 m as this is a practical distance for accessing the sample space; shorter distances start to become prohibitively difficult for using a number of different sample environments, as well as an oscillating radial collimator (see Section 4.6). Similar single-crystal diffractometers, e.g. MaNDI, iBIX, TOPAZ, use comparable L_2 distances (0.4–0.49 m).

In Section 4.4, $\Delta d/d = 0.0165$ was identified as the requirement for meeting the Key Driver. The effect of varying L_2 on angle-dependent time-of-flight resolution is shown in Figure 4.7 – obtained from fitting a simulated powder peak (d = 2 Å) at varying 2θ angles. The dotted horizontal line indicates the required minimum resolution. The vertical, red, shaded region shows the minimum 2θ value at which a *d*-spacing = 2 Å (another Key Driver) can be accessed using a 1-4 Å wavelength band. The Figure shows that L_2 = 0.5 m exactly meets the Key Driver at the smallest scattering angles. Above ca. 2θ = 40°, there is no clear advantage to extending L_2 beyond 0.5 m.

Also shown in the Figure are the (0 60 0) and (0 61 0) reflections (d = 2.0 and 1.967 Å) simulated as powder peaks at 2θ = 30° for L_2 = 0.5 m. There are two distinct maxima, though the peaks are heavily overlapped. However, in real biological crystals, systematic absences arising from space group symmetry mean that the simulation conditions shown here are likely to be overly-stringent: e.g. a common situation might mean that only reflections where $k = 2n$ for (0 k 0) are present. In the unlikely occurrence where two peaks cannot be clearly resolved at small 2θ angles, it remains an option to simply reorient the reflections towards larger 2θ angles where resolution improves. When the same two reflections are measured at 2θ = 40°, the peak splitting is much clearer. Resolution is doubled by 2θ = 55°, relative to 2θ = 30°

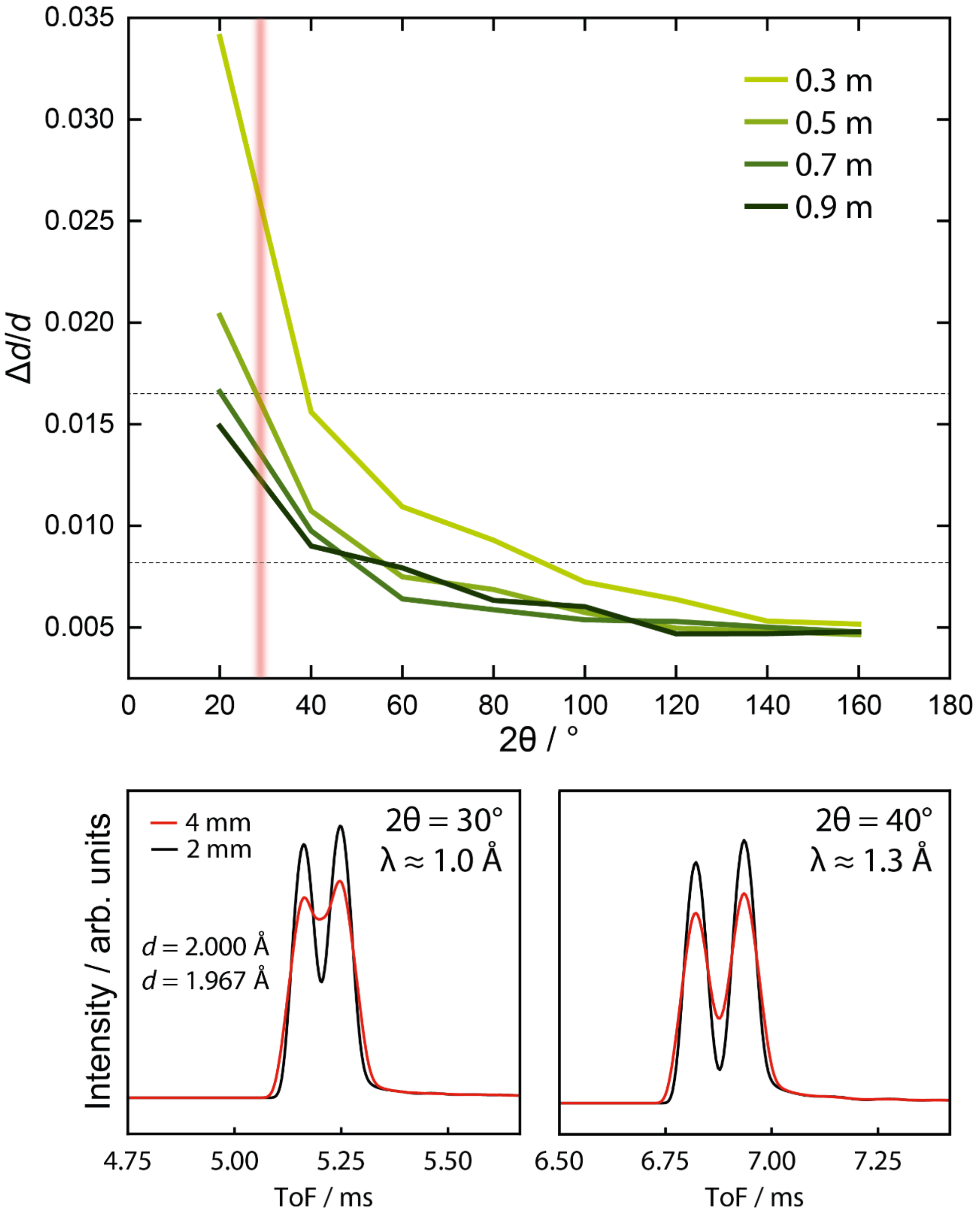

Figure 4.7. Top: Time-of-flight peak resolution Δ*d*/*d* as a function of scattering angle and L_2, using 4 mm detector pixels. The resolution is calculated as FWHM/*d* of a single diffraction peak. The horizontal dashed line shows the minimum Δ*d*/*d* requirement. The vertical, red, shaded region shows the minimum 2θ angle that *d* = 2 Å can be measured using the wavelength band available on the instrument. **Lower left:** (0 60 0) and (0 61 0) peaks (*d*=2.000 and 1.967 Å, respectively), simulated from a powder sample at 2θ = 30°, L_2 = 0.5 m. Red line shows a simulation results with a 4 mm pixel size, and the black line, 2 mm. Though overlapped (heavily for 4 mm), two peaks are distinguishable. **Lower right:** reorienting the same reflections to 2θ = 40° unambiguously splits the two peaks using either detector pixel size. Beam divergence was not actively controlled in these simulations, and uses the natural divergence of the instrument length with respect to moderator and sample sizes (ca. ±0.2°). The illuminated sample size was set to 1 × 1 mm.

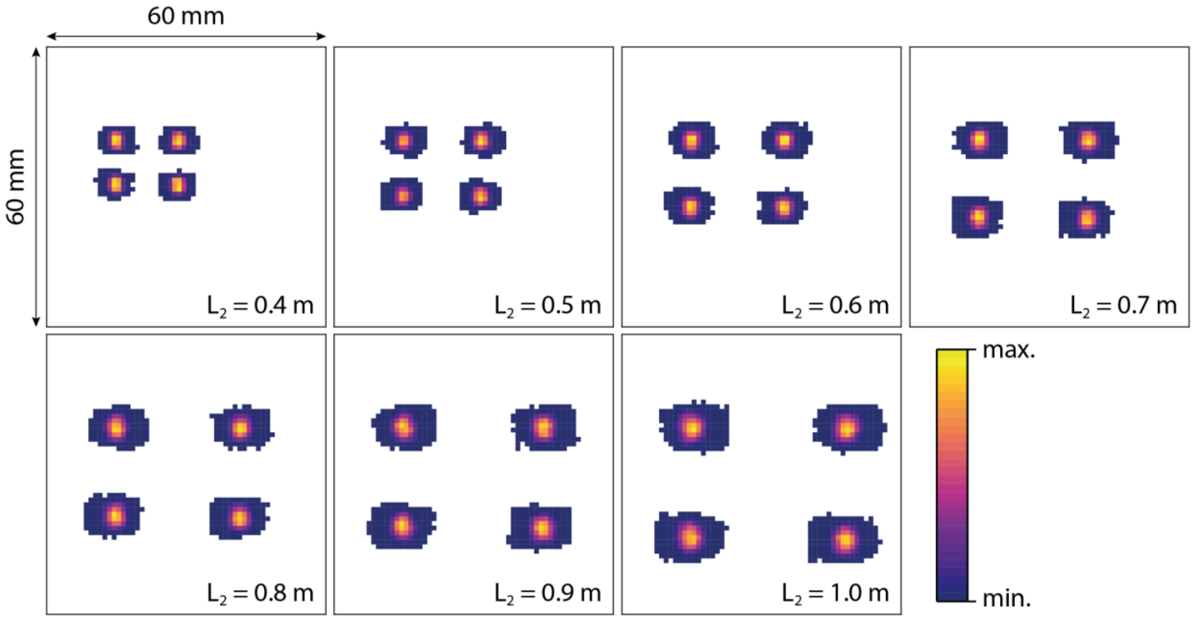

Figure 4.8. Reflection profiles at $2\theta = 90°$ with (0 60 0), (0 60 1), (1 60 0), and (1 60 1) Miller indices from a cubic unit cell with a = 120 Å. Each panel represents a detector area of 60 × 60 mm. Intensity values exactly equal to zero are coloured white, in order to highlight the full area occupied by the reflections. The L_2 distance is indicated in each panel.

Figure 4.8 shows the effect of varying L_2 on spatially resolving the (0 60 0), (0 60 1), (1 60 0), and (1 60 1) reflections. Pixel size is held fixed at 1 mm, beam divergence at ± 0.05° (which fully illuminates a pixel at L_2 = 0.5 m), and crystal mosaicity at 0.1° FWHM. In all cases, the four reflections are clearly resolved – increasingly with longer L_2, but the additional resolution is not necessary to meet the Science-Case-informed Key Drivers. Thus, Figure 4.7, and the L_2 distances used on other comparable single-crystal instruments are a more appropriate guide, indicating that L_2 = 0.5 m is the optimal length.

Following the internal review of the proposed LMX design, a recommendation was made to explore alternative detector arrangements. A simple but effective layout is a cylindrical 'barrel', where square panels can be easily tiled to provide large solid angle coverage – this is similar to the layout used on the SENJU instrument at J-PARC, and LADI-III at the ILL. The drawback is the increasingly oblique scattering angle made between the sample and detector towards the top and bottom of the cylinder. Simulations to assess spatial resolution at the uppermost edge of the detector (with overall cylinder height set at 0.768 m – see Section 5.5), along with the effect of varying pixel size, are shown in Figure 4.9. Panel **a)** in the Figure shows the profile of the four reflections with increasing pixel size. The peaks are unambiguously resolved – i.e. completely non-overlapped – up to 3 mm, but intensity maxima are still evident at 4 mm. Panel **b)** show the same four reflections, reoriented to the uppermost edge of the cylindrical detector arrangement (schematic shown in panel **c)**). Although the reflections cover an increased detector area, they can all still be resolved, even with a pixel size of 5 mm.

The double-layer wavelength shifting fibre (WSF) detectors that LMX will use offer the capability to electronically reduce the pixel size. Discussions with the ISIS detector group, and the simulations performed here, suggest that the best solution is to use 4 mm physical pixels that can be reduced to 2 mm, electronically. This then offers a choice between faster data collections (larger pixels) or increased resolution (electronic reduction) as required by the sample unit cell/symmetry. For 2 mm pixels, this places a lower constraint on beam divergence of ±0.12° to maximise beam flux.

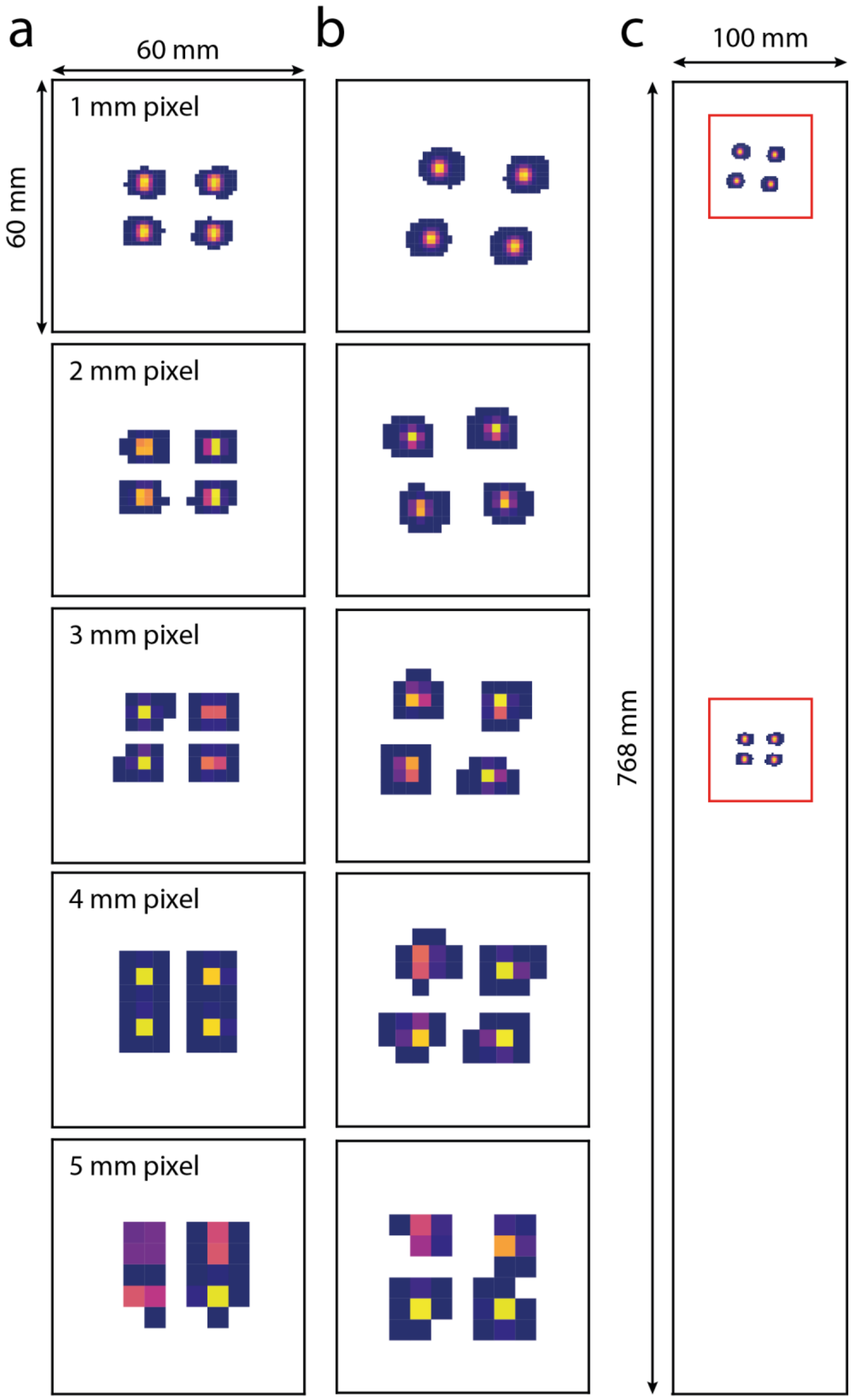

Figure 4.9. Reflection profile as a function of pixel size at **a)** the detector centre (ϕ = 0°) and **b)** top of the cylindrical detector arrangement (ϕ ≈ 36°). **c)** Schematic of the relative reflection positions on the detector face. The pixel size indicated in **a)** also applies to the adjacent panel in **b)**. Intensity values exactly equal to zero are coloured white, in order to highlight the full area occupied by the reflections.

4.6 Minimising background

The chemical crystallography component of the LMX science case requires non-ambient sample environments, e.g. CCR/furnace, which have additional shields for thermal insulation/vacuum. A common means of removing parasitic scattering is an oscillating radial collimator (ORC). An example is shown in Figure 4.10 from the newly-installed ORC on SENJU at J-PARC, where its installation significantly improved data quality for measurement in sample environment (a cryostat in the Figure). Neutron single-crystal instruments at other international facilities vary in whether they use an ORC or not. In some cases, e.g. D10 (ILL), simply the use of sample environment shields that are commensurate with detector geometry (see Figure 4.10) proves sufficient, so that path differences through the shield for scattered neutrons are minimised.

Following consultation with instrument scientists on MaNDi, TOPAZ (SNS) and SENJU (J-PARC), LMX will use a removable ORC, compatible with standard sample environment. This would need to be a small-profile collimator, supported on a single post so that detector coverage is not compromised – detectors at the base of instrument would be used when the ORC is removed. Engineering effort will be required to realise/develop this design.

LMX will not use an evacuated sample tank – it presents logistical challenges in combination with a goniometer arm and a vacuum cannot be used in conjunction with a cryostream, which forms at least half of the scientific programme (covering temperatures 100–500 K). Other macromolecular instruments such as MaNDi (SNS) and iBIX (J-PARC) do not use a sample tank for similar reasons. Discussion with scientists on the TOPAZ instrument (SNS) revealed that although they possess a vacuum tank, it is rarely used, only having a minimal effect on the quality of the diffraction pattern once air scatter is removed.

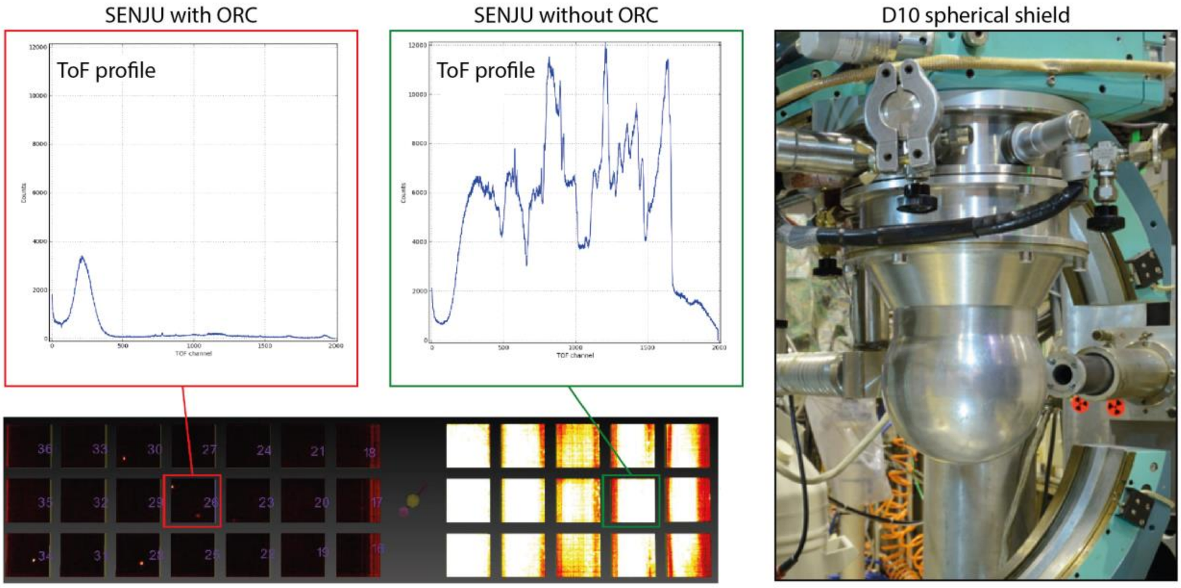

Figure 4.10. Left: individual detector diffraction images, and a selected time of flight profile from the SENJU instrument using the ORC with a cryostat. **Centre:** without the ORC, backgrounds are substantially higher. **Right:** a spherical shield in use on D10, ILL. SENJU images courtesy of Takashi Ohhara.

4.7 Sample line-of-sight and activation

Biological crystals are fragile and their sensitivity to synchrotron radiation is well-documented. Several existing, and proposed, neutron instruments (MaNDi, LADI-III, NMX) break direct line of sight between the sample and the moderator using curved guides, to avoid prompt gamma radiation. LMX does not have a sufficiently long flight path to achieve this with a curved guide. Moreover, a curved guide would complicate transport of the short wavelength (ca. 1 Å) neutrons that will be important to the chemical crystallography programme.

Discussions with the ISIS neutronics group (Steven Lilley) indicated that prompt gamma originating from the area local to the sample (e.g. sample environment) is likely to represent a more potent source, rather than direct gamma radiation from the moderator. This being the case, it is likely that the extent of 'local-area' prompt gamma would be similar for other neutron instruments without a direct line of sight. Furthermore, ISIS TS1 is a significantly lower-power source than the SNS, ILL, or ESS where the instruments above are (or will be) based.

Sample damage is not anticipated. Nevertheless, as a mitigation strategy, a t_0 chopper positioned in a 1 m gap before the start of the guide (ca. 0.5 m required) prevents this situation, as well as allowing measurement of the desired wavelength range over two time frames, as discussed in Section 4.4. Following the internal review of the proposed LMX design, the re-evaluated (now elliptical) guide geometry has a smaller opening than the previous design. This brings two benefits with respect to gamma/fast neutron irradiation: i) the direct view of the moderator face from the sample position has been greatly reduced, and ii) the sweep time of the t_0 chopper has been reduced (to 6.5×10^{-4} s) from that required from the previous guide design.

4.8 Summary of design options ruled out

Moderator: Hydrogen is the preferred moderator material over methane or water due to its much larger flux over the crucial waveband for the LMX science case. TS2 hydrogen is ruled out relative to (refurbished) TS1 because it has lower brilliance, a slightly broader time structure, but crucially TS1 benefits from the higher 40 Hz repetition rate.

Primary flight path: The instrument needs a time resolution $\Delta t/t$ better than 0.0165 to meet the science case; this can be achieved with an 8 m instrument, but the long tails of the peaks mean that FWHM is an unreliable metric for judging resolution. A longer instrument is prudent for resolving peaks, but also for removing background; spreading it over more time channels assists its removal. The 19.5 m L_1 length simultaneously meets several criteria:

i) exceeds time resolution
ii) separates background signal
iii) is commensurate with the desired 4 Å waveband
iv) remains within the physical confines of the TS1 building.

Neutron transport: Following internal review, a re-valuation of the guide options indicates that an elliptical guide would be superior to the previously-proposed square, linear guide. The square, linear guide does offer excellent brilliance transfer, but it does also transport many unwanted neutrons outside of the sample dimensions. The elliptical guide proposed here provides comparable brilliance transfer, while reducing the beam size – transporting less unwanted phase space and allowing faster chop times.

Sample-to-detector distance: A shorter L_2 than 0.5 m was ruled out because it does not allow sufficient operating space around the sample. Although a longer L_2 provides improved spatial resolution, it exceeds the requirements of the Science Case and would require a greater quantity of detectors, increasing the cost.

5) The proposed instrument design

5.1 Instrument overview

Summary: TS1 H_2 moderator, elliptical guide, *t_0* chopper, two single-disc frame overlap choppers, pre-guide slit, two post-guide jaw sets, beam scraper, no evacuated sample tank, 3π detector coverage.

The schematic of the proposed instrument is shown in Figure 5.1. The primary flight path is 19.5 m and consists of a t_0 chopper to remove prompt gamma, two single-disc choppers to select the wavelength band, a 11 m elliptical guide, a 1 m section of beam scrapers, with jaws at each end to shape the incident beam profile. The sample position is surrounded by double-layer, wavelength-shifting fibre detectors, covering as large a solid angle as possible, in a cylindrical arrangement, with the shortest L_2 being 0.5 m from the sample. A removable oscillating radial collimator (ORC) reduces background scattering from sample environment. A removable boronated beam snout and get lost pipe can be inserted to reduce background scattering (with or without the ORC). A retractable goniometer arm, nitrogen cryostream and video camera comprise the remaining components in the sample space.

The various components of the instrument are discussed in more detail in the following sub-sections.

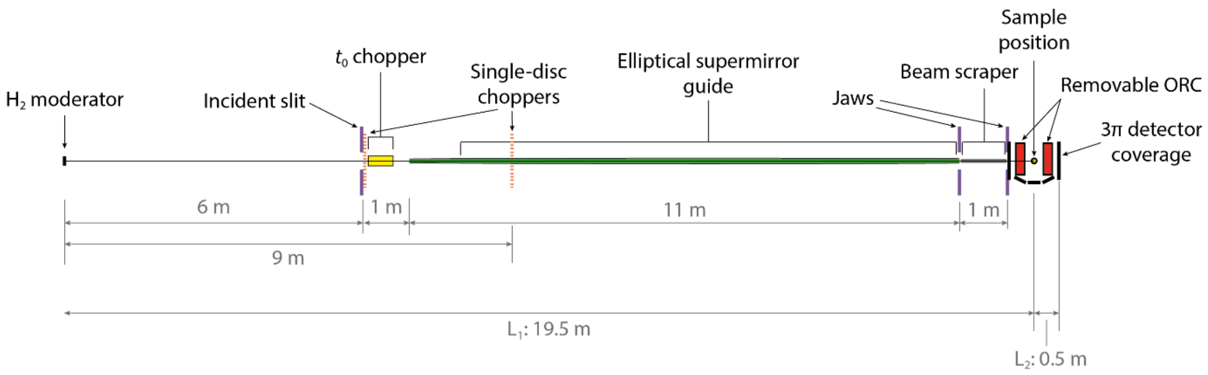

Figure 5.1. Scale schematic of the LMX instrument (side view). Incident beam components are labelled on the diagram, and relevant dimensions are given below it.

5.2 Guide

11 m elliptical guide, starting at 7 m from moderator and ending 1.5 m from sample. Guide opening 0.018 m, ellipse mid-point 0.035 m.

One of the Key Drivers is to transfer high brilliance across the desired wavelength range. The previous LMX design used a square, linear guide measuring 7.5 × 0.079 × 0.079 m, which had near-100% brilliance transfer across the 1–5 Å wavelength band for neutrons with ±0.4° divergence. Though this design is very effective, it has the following drawbacks: i) transports a significant number of neutrons outside the target sample dimensions (i.e. background scattering); ii) has a large direct view of the moderator (transporting undesirable gamma radiation – see Section 4.7); iii) requires increased chop times due to the large guide opening. Though the first of these (i) can be mitigated with jaws, it is undesirable to transport these neutrons in the first place. Note that all brilliance transfer calculations/plots shown in this section assume a sample size of 2.5 × 2.5 mm and beam divergence ±0.4°.

A recommendation from the LMX internal review was to explore the potential benefits of an elliptical-focussing guide (see Appendix). The guide geometry places the focal points of the ellipse at the sample position and at the edge of the shielding wall, 6 m from the moderator face. A set of slits at L_1 = 6 m controls the view of the moderator at the guide entrance. Panel **a)** in Figure 5.2 shows the new proposed guide geometry.

The effect on brilliance transfer of starting/ending the guide entrance/exit at varying distances from the ellipse focal points is shown in Figure 5.2, panel **b)** – the overall integrated neutron intensity is used as a figure-of-merit. For each distance increment shown, a separate set of simulations were carried out, systematically varying the ellipse mid-point height. The result producing the largest brilliance transfer values are plotted here. The position of the guide entrance shows invariance with distance ≥ 7 m. It is desirable to extend the guide closer to the moderator – the smaller guide opening leads to shorter chop times, and fewer discs required (see Section 5.3 – ca. £200k saved). 7 m is therefore the optimum moderator-to-guide-entrance distance. The guide-exit-to-sample distance shows that brilliance transfer increases as this distance decreases. The plot for guide exit distance indicates that this should be as short as possible, however, it is necessary to accommodate two jaw sets and a frame overlap mirror, ahead of the sample space (which begins at 19 m). A 1 m gap is necessary to allow sufficient space for these components – i.e. a distance of 1.5 m between the sample and guide exit. The corresponding wavelength–divergence diagram for these optimised dimensions is given in Figure 5.2, panel **c)**, showing minimal structuring in transported neutron divergence.

In all simulations, a maximum sample size of 2.5 × 2.5 mm is used – realistic sample sizes will be smaller than this

The jaw sets indicated in Figure 5.2 **a)**, shape the beam divergence reaching the sample. The pre-guide set of slits (at 6 m) does not narrow to the focal point of the ellipse, as doing so restricts some of the direct view of the moderator from the sample, resulting in some divergence structuring that reduces beam homogeneity.

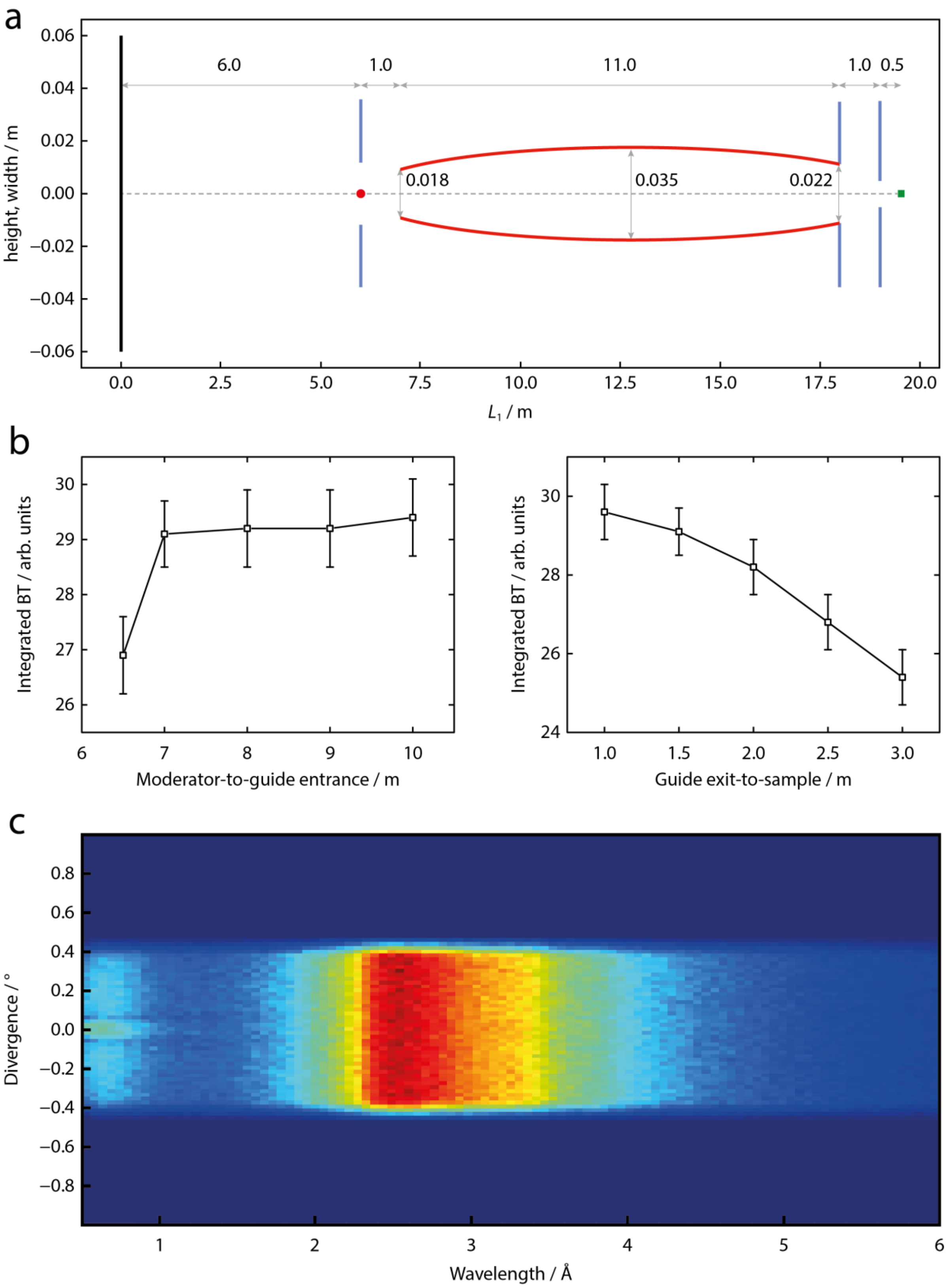

Figure 5.2. a) Schematic of guide geometry, showing ellipse focal points at 6 and 19.5 m, slit/jaw sets and moderator face. **b)** Integral of brilliance transfer (figure-of-merit) for varying guide geometry. **c)** Wavelength–divergence diagram of neutrons transported by guide to sample position. The small rise in intensity at short wavelengths with low divergence arises from the direct view between the sample and moderator.

The original motivation for exploring an elliptical guide was to transport fewer unwanted neutrons outside the sample dimensions, while maintaining good brilliance transfer. Figure 5.3 shows the profile of the neutron beam at the sample position, using the previous square, linear guide, compared with the elliptical guide. Figure 5.4 shows brilliance transfer as a function of wavelength and *m*-coating – the performance is comparable to the square, linear guide (see Appendix). It is clear that for λ ≥ 1 Å, there is negligible difference between *m*-grades 3–5, and these transport ca. 80% of short-wavelength neutrons, rising to ca. 98% by 1.5 Å.

The distribution of neutron reflections across an elliptical guide is not uniform, so a calculation of the required *m*-grading at discrete sections of the guide has been performed, so as to minimise unnecessary cost. The result of the calculation is shown as a contour plot in Figure 5.4; the number of reflected neutrons is plotted versus position along the guide length (shown as an absolute value along the full beam path), versus the *m*-grade required to reflect the neutrons. The top right panel of the plot summarises the *m*-coat grade required to transport 95% of neutrons as a function of guide length – the ends of the guide require $m \approx 3.5$, and the guide centre $m = 2.4$.

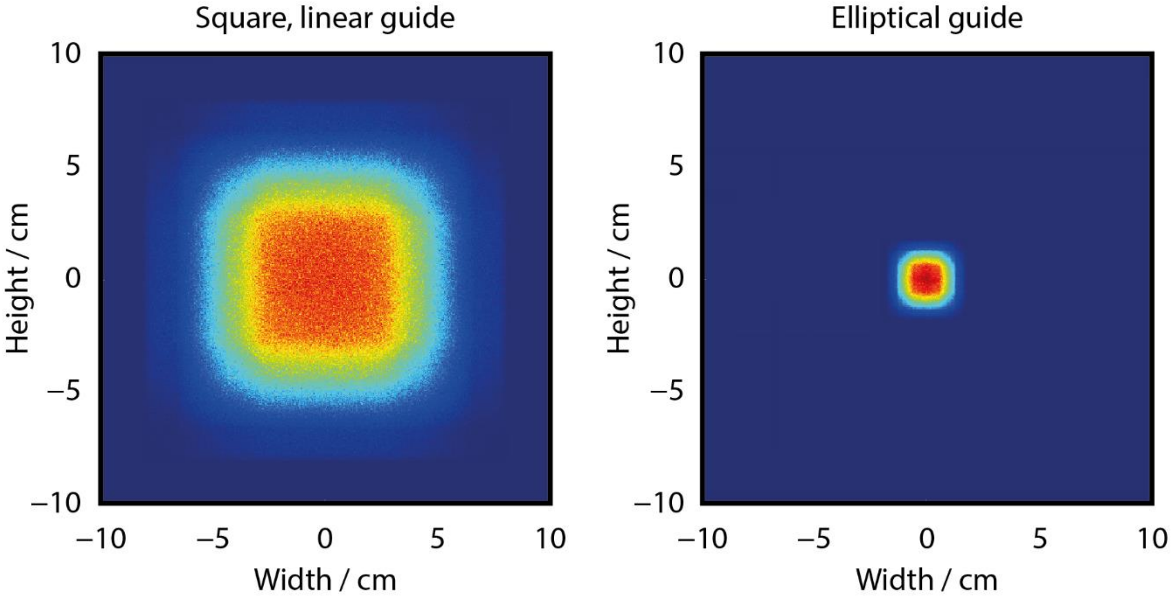

Figure 5.3. Beam profile at the sample position using (the previously proposed) square linear guide (left), and revised elliptical design (right). A large beam divergence (±5°) was allowed to better observe the extent of unwanted neutron transport. The elliptical guide is superior in focussing the beam towards the sample dimensions, when compared with the square, linear guide, thus reducing background scattering. Further shaping of the beam profile is achieved through jaws sets and pinhole collimators (see Section 5.4).

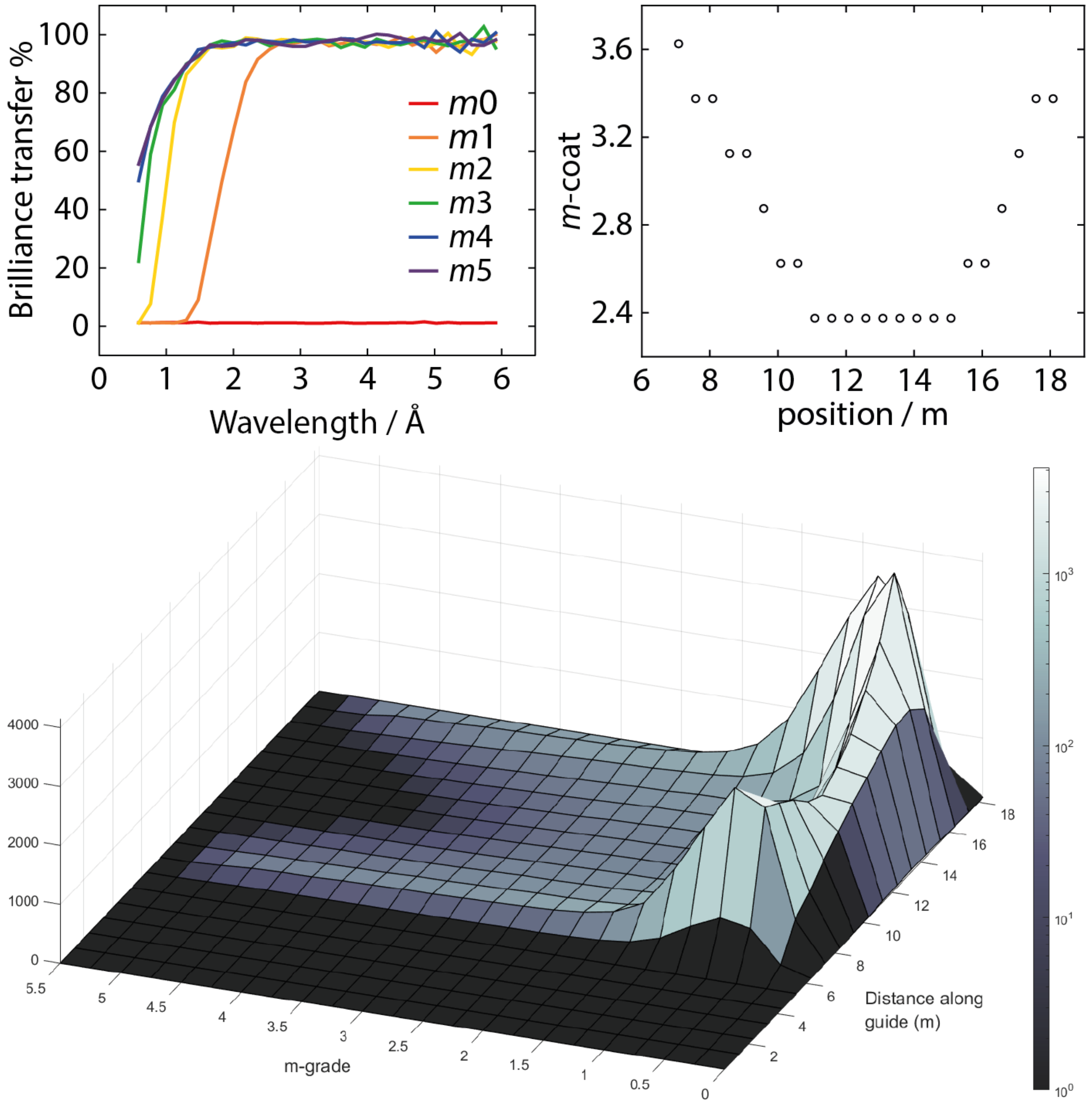

Figure 5.4. Top left: brilliance transfer as a function of *m*-coat and wavelength, using a sample size of 2.5 × 2.5 mm and ±0.4° beam divergence. **Top-right:** *m*-coating at position along primary flight path, required to transport 95% of neutrons. **Lower:** contour plot showing number of reflected neutrons versus position along guide versus *m*-grade. Zero values are set to black.

5.3 Choppers

50 Hz, 0.35 m radius, single-disc choppers at 6.0 m (opening 109.3°) and 9.0 m (opening 164.2°). t_0 chopper positioned after first single-disc chopper

A t_0 chopper is included to remove the prompt gamma pulse from reaching the sample position. A standard t_0 unit requires approximately 0.5 m of space to accommodate it – this will be located as close to the biological shielding wall (L_1 = 6 m) as possible.

In order to deliver a wide wavelength band across $L_1 + L_2$ = 20 m, while minimising contamination of frames with long wavelength neutrons, chopper positioning was initially guided by a phase space diagram – see Appendix. Following the LMX internal review, a recommendation was made to relocate the choppers to 6, and 9 m. This has the effect of removing an increased proportion of unwanted long-wavelength neutrons, overlapping with another frame. Therefore the t_0 chopper will be placed immediately after the first single-disc, frame overlap chopper.

McStas (2.7.1) simulations were performed using a flat-intensity source and a wavelength monitor at the sample position. Chopper dimensions were informed by ISIS chopper design engineers, using a disc radius = 0.35 m, disc centre–guide centre = 0.25 m, and a unit width of 0.035 m. Both choppers were set to operate at 50 Hz. In order to transmit the 4 Å wavelength band while in a fully open orientation, chopper apertures of 109.3° and 164.2° were required for positions at 6.0 and 9.0 m, respectively. These calculations were based on the elliptical guide geometry detailed in the next section.

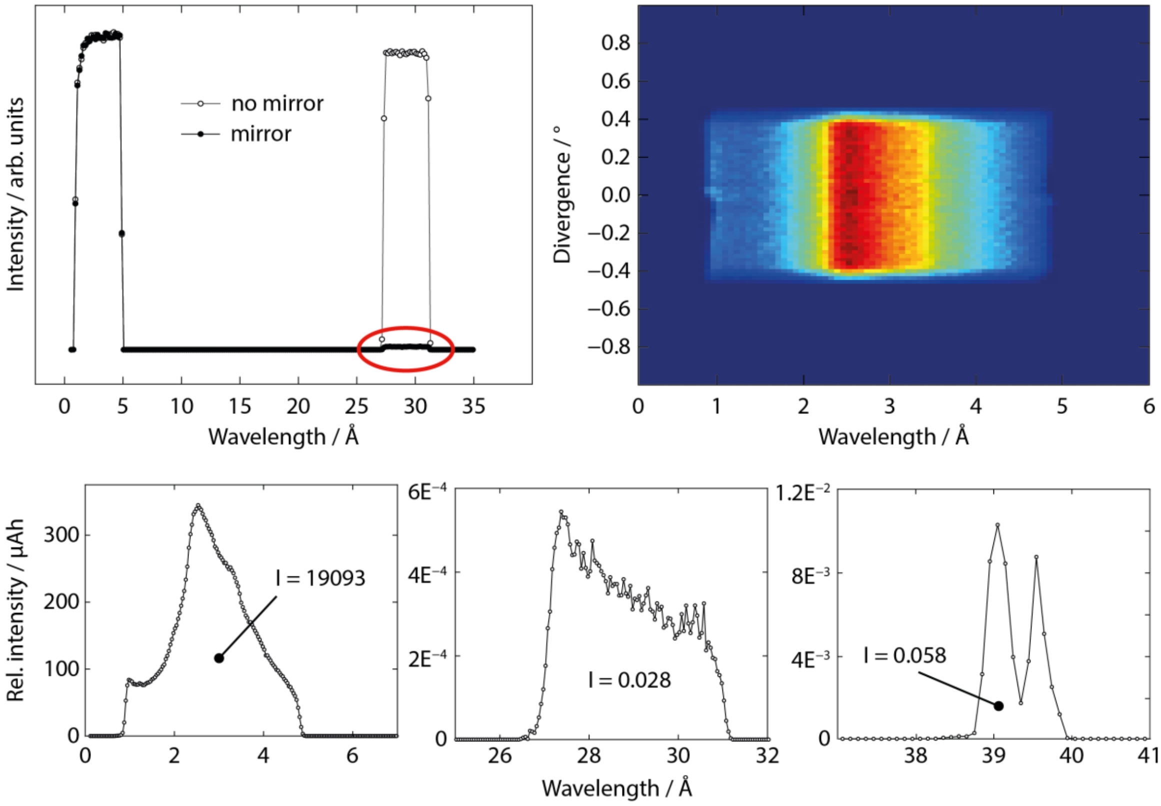

Figure 5.5. Top-left: neutron wavelengths reaching the sample, simulated using a uniform-intensity source. The effect of the frame overlap mirror is indicated by the red circle. **Top-right:** divergence–wavelength profile of neutrons reaching the sample position, determined by the chopper geometry. **Lower row:** respective intensities of simulated neutrons reaching the sample, using the TS1 H_2 moderator component and frame overlap mirror.

The first contaminant neutrons to reach the sample position occur between ca. 26–31 Å. These can be effectively removed with a frame overlap mirror, positioned between the final two jaw sets. Figure 5.5 shows the effect of its inclusion. In order to fully span the neutron beam, the mirror is 0.7 m long, and inclined by 2° with respect to the primary beam direction, occupying a total distance along L_1 of 0.69 m. A supermirror coating of m = 1.5 results in near-complete suppression of the long-wavelength neutrons. The respective integrated intensities of the neutrons reaching the sample, simulated using the LOQ view of the TS1 H_2 moderator, are also shown in the Figure – the unwanted neutrons have negligible intensity and can safely be ignored.

The wavelength–divergence profile of the neutrons reaching the sample, within the desired wavelength range, is also given in Figure 5.5. Compared to the profile seen with the square, linear guide design (which used double-disc choppers – see Appendix), the smaller gap in the elliptical guide required to accommodate the single-disc chopper results in a more homogenous beam with respect to divergence.

Figure 5.6 shows the distance–time diagram for the chopper geometry. Also shown in the Figure are the neutron wavelengths that reach the sample position during the chopper opening and closing times (grey bands). Due to the smaller beam dimension provided by the elliptical guide compared to the previous design, chop times are improved, while also being able to use single-disc instead of double-disc choppers. The chop times result in a usable waveband of 3.8 Å (0.019 s) cf. 3.6 Å with the previous chopper arrangement.

Lastly, the sweep time of the t_0 chopper, positioned at ca. 6 m from the moderator was calculated for the guide geometry discussed in Section 5.3. The t_0 chopper uses 'standard' dimensions, informed by the chopper group at ISIS; a disc-centre-to-beam-centre distance of 250 mm, and a blocking blade 3 mm wider than the guide aperture. The total calculated sweep time is 6.5×10^{-4} s, which corresponds to 3.3×10^{-4} s either side of the prompt pulse. This means wavelengths below 0.22 Å will be unmeasurable, however this is safely below the desired wavelength minimum, and this is show schematically in Figure 5.6.

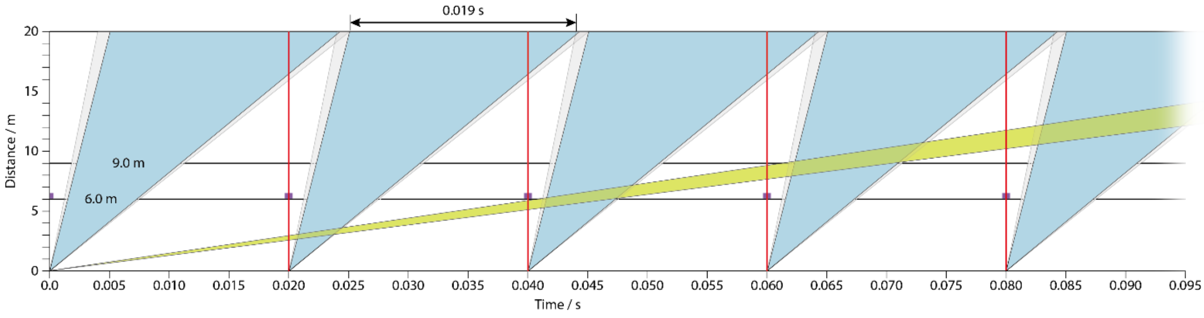

Figure 5.6. To-scale chopper distance/time diagram. Solid black horizontal lines at 6 and 9 m show the time regime over which the choppers are closed. Vertical red lines indicate the 50 Hz repetition rate on TS1. Blue bands show the neutron time-of-flight transmitted by the choppers when fully open. The grey bands indicate additional neutrons that pass through the choppers as they are opening/closing. Ultimately, this leads to a 0.019 s (3.8 Å) time region that is free of any overlap with other neutrons. The green band shows the first band of long-wavelength neutrons reaching the sample. The small purple blocks at ca. 6 m indicate the sweep time of a potential t_0 chopper.

5.4 Shaping the beam profile

Square B_4C jaws positioned at 18, and 19 m. Removable pinhole collimation at 19.47-19.48 m

The instrument will use a very straightforward jaws system to shape the beam – one positioned at the guide exit (L_1 = 18 m) and the second at the start of the sample space (L_1 = 19 m). The height and width will be constrained to be the same and allow a beam size up to 2.5 × 2.5 mm at the sample position, in line with one of the Key Drivers. Ultimately the beam size will be tuneable down to very small sample sizes (sub mm^3). The evacuated beampipe between the jaw sets (1 m) will consist of absorbing scraper blades to ensure only transmission of the desired beam divergence.

Between the second jaw set and the sample position, the beam will be transported by a removable boronated snout (located on a kinematic mount), to minimise any unwanted scattering ahead of the sample position. In order to minimise background scattering, a final pinhole collimator will be located in the end of the snout immediately before the sample. The design will be similar to that used on the MaNDi instrument at the SNS (Figure 5.9) where the collimator is a removable boron nitride piece (ca. 1 cm in length), inserted in the end of the boronated snout. A number of different pinhole sizes will be available so that the beam profile can be more closely matched to the sample geometry. Historically, this has been shown to be effective on both SXD (ISIS) and D9 (ILL). Figure 5.9 shows the beam geometry for a 2 cm diameter collimator piece, located 2 cm from the sample position. This leads to some occluded detector coverage in backscattering geometry: ca. 0.36 steradians. Removability enables the use of different length snouts (in conjunction with appropriately-sized pinhole collimation), affording more flexibility for sample environment. Shorter/thinner snouts will result in reduced detector occlusion – the worst-case scenario is presented here. For chemical samples, snout removal will permit access to back-scattering detectors, which will become more important for measuring diffraction from shorter wavelength neutrons.

Figure 5.10 shows the simulated beam profile at the sample position using a range of divergence acceptance, and pinhole collimation to shape the beam. The size of the collimator diameter is selected to i) match the sample size, ii) permit a ±0.4° beam divergence, and iii) be a realistic value for machining/practical use.

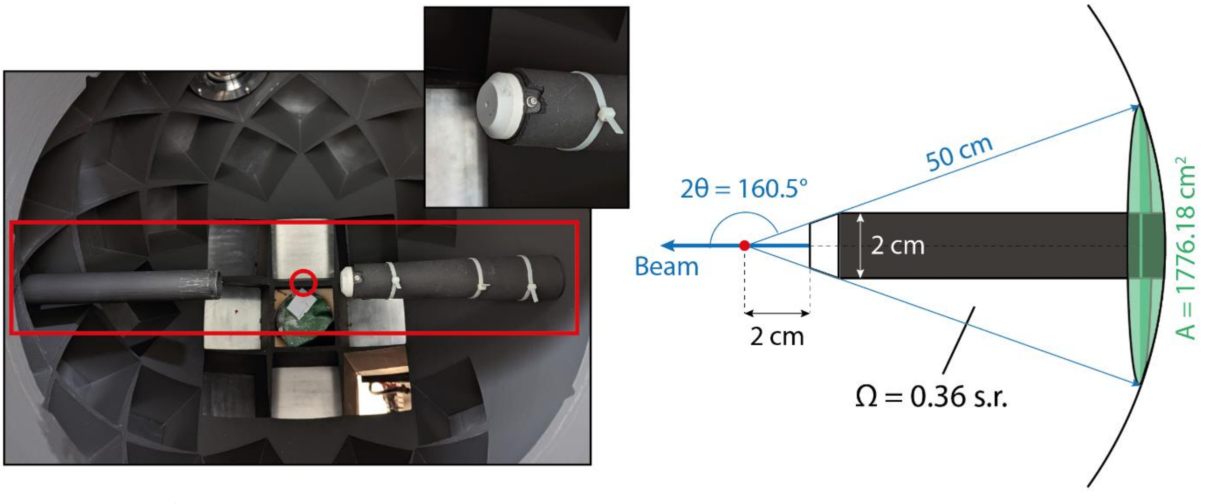

Figure 5.9. Left: MaNDi detector tank with red box highlighting get lost pipe, approximate sample position (circle) and boronated snout. The inset graphic shows a zoomed image of the snout, which contains a boron nitride pinhole collimator, inserted in the end. **Right:** Schematic showing the beam occluded by the snout indicates an occluded spherical cap area of 1776 cm^2 (green) and a solid angle reduction of ca. 0.36 steradians. The thick blue arrow shows the transmitted beam through the sample (red dot), and the thin arrows show the maximum possible diffracted beam angle.

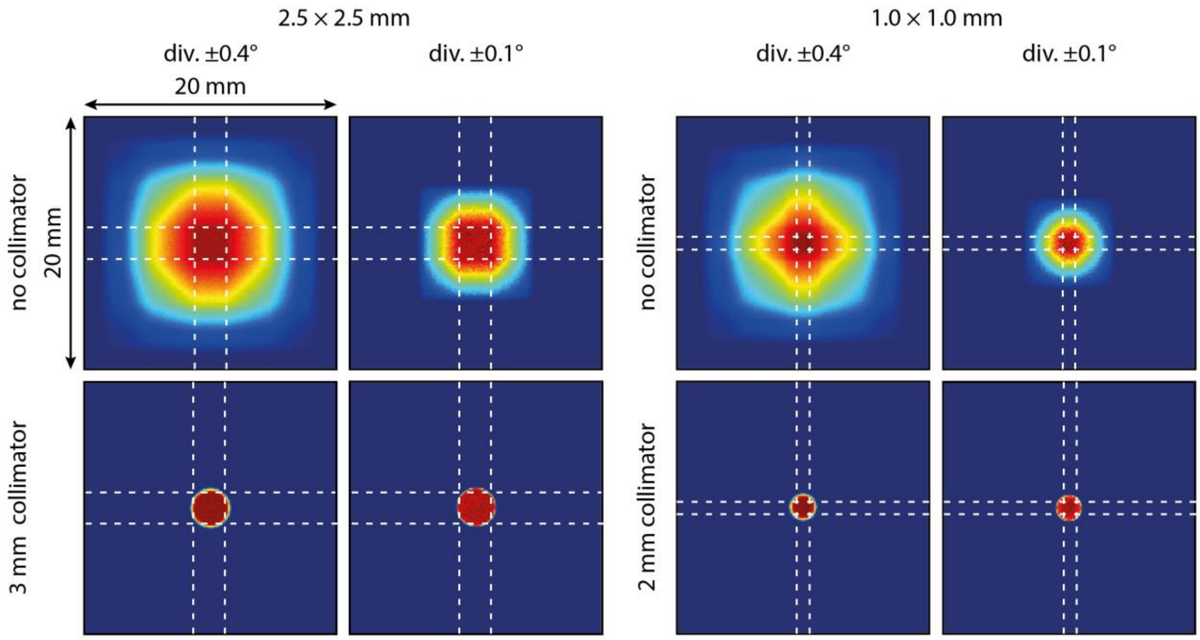

Figure 5.10. Beam profile at sample position without (top row) and with a pinhole collimator (bottom row). The jaws are set to accept beam divergence of either ±0.4° or ±0.1° for samples measuring 2.5 × 2.5 and 1.0 × 1.0 mm (columns). The dashed white lines indicate the sample dimensions.

5.5 Sample space

Ca. 3π sr, cylindrical, detector coverage with $L_2 \approx 0.5$ m, sample goniometer, cryostream, Tomkinson flange. *Note: this section requires design effort for full evaluation*

The original LMX detector layout proposed a near-spherical arrangement of square detectors, positioned 0.5 m from the sample, aiming to cover as large a solid angle as possible.

Following review, two alternative designs were suggested by the review panel: i) the WISH-II instrument concept, which also aims for large detector coverage using a nominal solid angle of 8.4 sr, using a combination of square and triangular detector panels, and ii) a cylindrical 'barrel'-type design comprised of square panels only (similar to the arrangement used on SENJU and LADI-III). The latter is particularly appealing, owing to its engineering simplicity – shown in Figure 5.11. In combination with angled square, and rectangular detectors on the base, it covers a solid angle of 9 sr (for a 0.5 m radius and cylinder height of 0.768 m) as well as providing a geometry that is more commensurate with an oscillating radial collimator (ORC). The array encompasses a total of 44 detector panels.

The potential drawback of the cylindrical layout is the variable L_2 and oblique scattering angle that becomes more severe toward the top and bottom edge of the detector. Neither of these are likely to prove serious issues – a lack of spatial overlap at the edge of the cylinder was evident from simulated reflection profiles presented in Section 4.5. However, the situation is exacerbated by the fact that the individual faces in the double-layer detector modules are separated by 4 mm, and it is not currently possible to identify which of the layers the scattered neutron strikes; this leads to a difference in the apparent height of the detected neutrons. Figure 5.12 shows simulations with a 4 mm difference in detector position, showing that while this effect does result in a slight elongation of the detected neutron, all reflections can be clearly resolved when using 2 mm pixels. The elongation of the reflection profile is not an issue for data processing; the current integration routines in the Mantid software simply look for regions of continuous scattering density.

The cylindrical geometry would additionally prove a complementary shape to existing sample environment (e.g. CCR/furnace). With the use of a cylindrical geometry, there is a reduced need to use a smaller flange diameter, as was proposed for the previous LMX design. Use of a standard Tomkinson flange allows LMX to take advantage of existing equipment from day one of operation, and removes one of the technical risks associated with the instrument.

The single-crystal samples will be mounted in one of two different ways – either in sample environment (CCR/furnace) loaded through the top of the instrument, or on a retractable, side-loading goniometer arm, either for measurement under ambient conditions or use with a nitrogen cryostream. The latter scenario (goniometer and cryostream) is envisaged to comprise upwards of 50% of the measurements performed.

Following consultation with instrument scientists on the MaNDi and TOPAZ instruments at the SNS, there is no clear need for an evacuated sample tank; the background for any biological samples will be dominated by hydrogen content in the sample, and any chemical samples measured in sample environment will use vacuum chambers built onto the equipment itself. Where vacuum/heat shields are in use, LMX will have an option to use an ORC to reduce parasitic scattering, optionally in conjunction with a shortened incident beam snout (see Section 5.4). Support on a single post mount is the most likely solution to avoid compromising detector coverage at the base of the cylinder.

A side-loading goniometer arm will be translated in and out of the instrument on a motorised stage, and access will also be required for a video camera (sample alignment) and a removable cryostream.

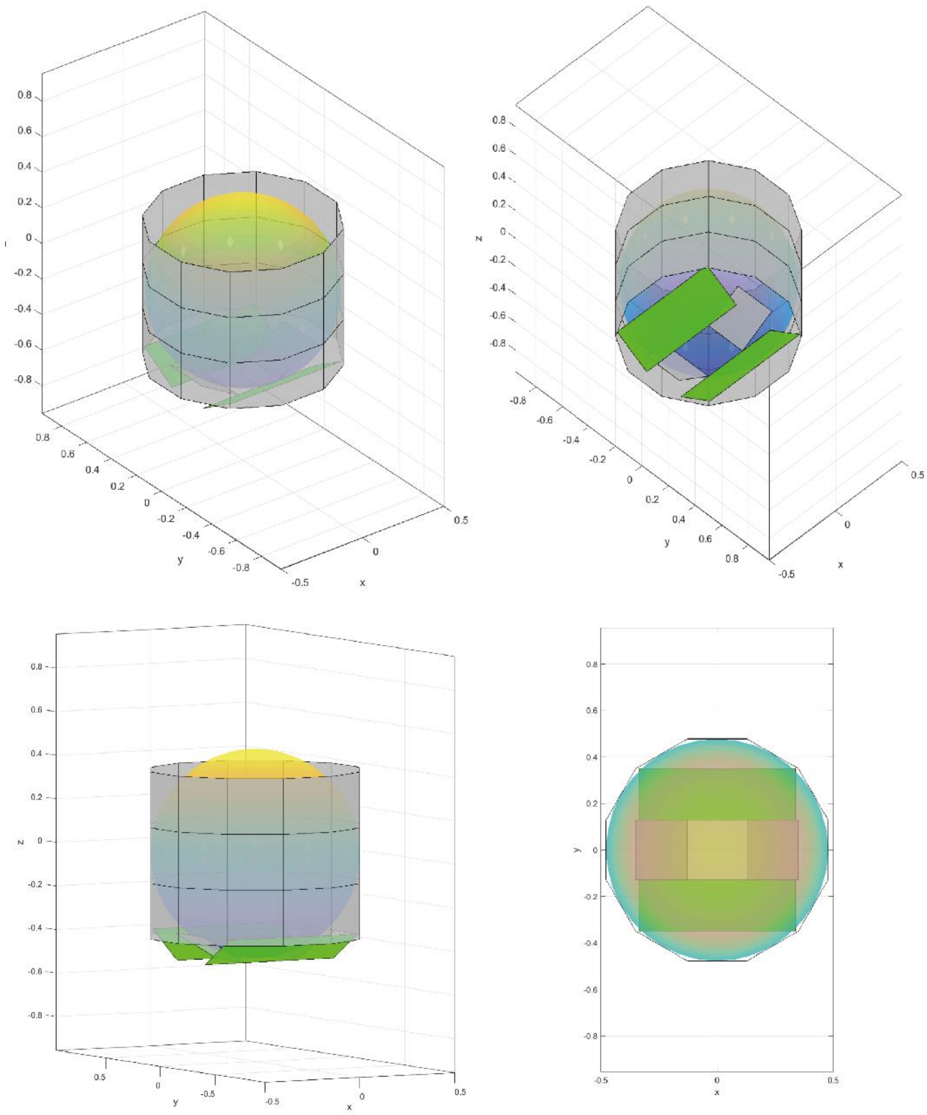

Figure 5.11. Cylindrical detector layout concept. Each panel measures 0.256 × 0.256 m. Cylinder height is 0.768 m, and radius is 0.5 m. Near-isometric views are shown from above (top left), and below (top right) the detector array. Side-on view is shown in the bottom left panel, and the view from directly above is shown in the bottom right. A gap has been left at the centre of the base to allow space for the envisaged ORC support post. The green panels show a rectangular array (comprised of 3 square panels) of detectors at the base of the instrument, inclined towards the sample, to maximise detector coverage.

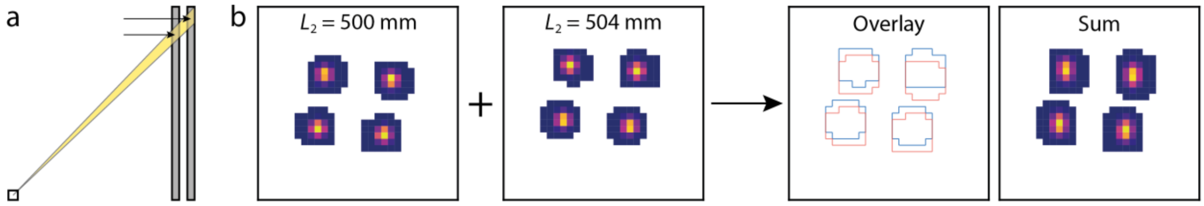

Figure 5.12. a) Schematic of the parallax effect with diffracted neutron beam striking detecting layers at two different distances. The arrows indicate the relative heights of the detected neutron rays. **b)** McStas simulations using the same reflection geometry in Figure 4.9, but placing a detector at 500 and 504 mm from the sample position. Summing these together shows slight reflection elongation, but the individual reflections continue to be resolved using 2 mm pixels.

5.6 Detector technology

LMX will use the newly-developed double-layer, wavelength-shifting fibre detectors, detailed in Mauri et al, *J. Appl. Crystallogr.*, (2024), **57**, 1-10. These are highly efficient detectors across the wavelengths that LMX will measure – these are plotted in Figure 5.13. Efficiency is comparable to the Anger cameras in use at the SNS, but gamma sensitivity is approximately 4 orders of magnitude lower. Each panel will use 4 × 4 mm pixels (electronically-reducible to 2 × 2 mm), with 64 fibres leading to panel dimensions of 256 × 256 mm. The detectors that comprise the rectangular sections on the base of the array will use either 56 or 57 fibres, giving edge lengths of 224, and 228 mm, respectively.

Extensive testing of a prototype single-layer module, installed on SXD during 2020, shows a ca. three-fold increase in efficiency over the current ZnS scintillation detectors. The double-layer option has recently been tested on SXD where count rates from a NaCl standard show improvement by a factor of 3.5, and 4 for the (2 −4 2) and (4 −8 4) reflections (λ = 2.2 and 1.1 Å), respectively, when compared with the previous SXD detector technology.

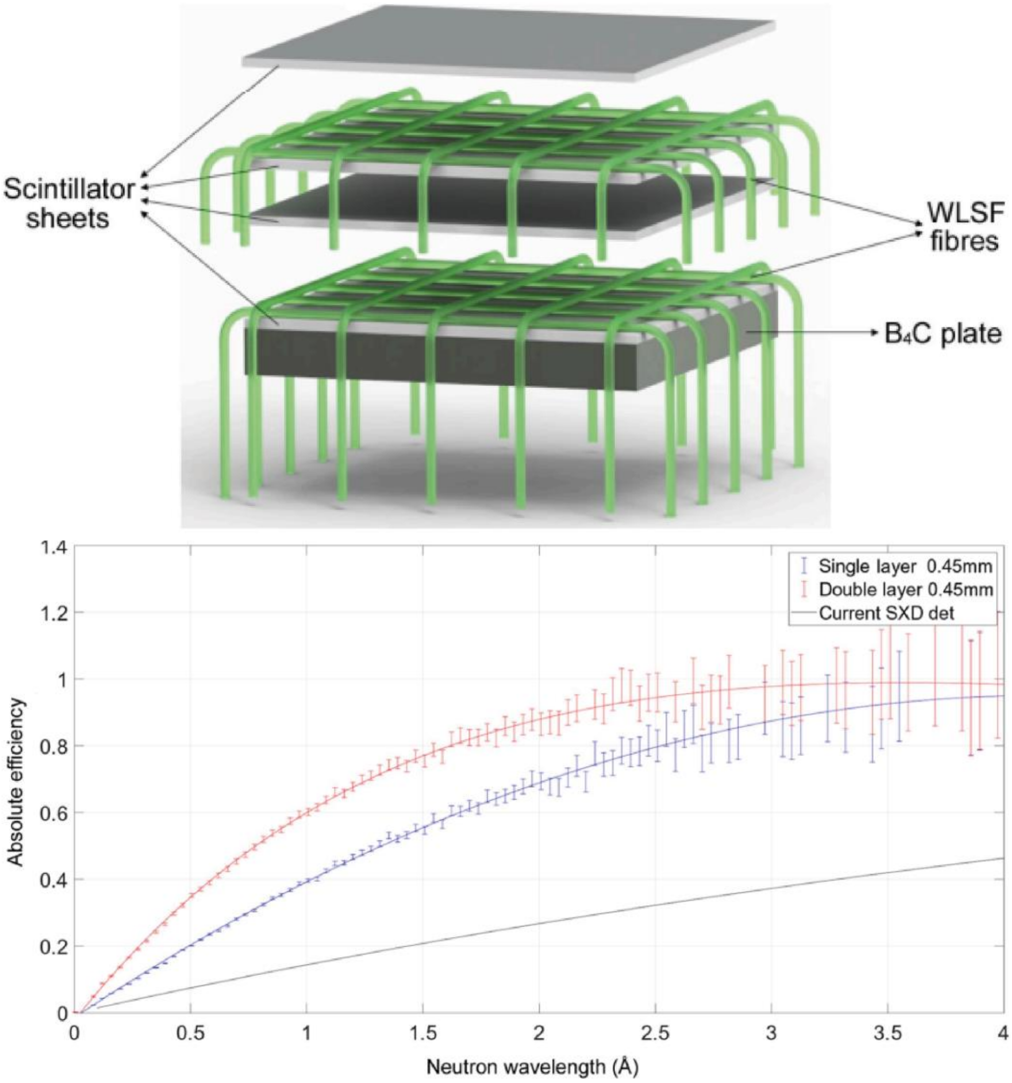

Figure 5.13. Top: Double-layer WSF detector unit. **Bottom:** detector efficiency as a function of wavelength, benchmarked against the current SXD detectors. Images taken from *J. Appl. Crystallogr.*, (2024), **57**, 1-10

6) Performance comparison

6.1. New measurement capability and timescales

LMX is a new neutron instrument at ISIS, offering a completely new capability and therefore cannot be easily benchmarked against any existing instrument at ISIS. The most straightforward comparison is to contrast its anticipated performance against another large-molecule single crystal diffractometer at a time-of-flight source. The MaNDi instrument at the SNS is the best comparator though LMX has a shorter primary flight path and a lower-power source. Both instruments have a similar L_2, beam divergence, and detector pixel size.

LMX uses a wider waveband than MaNDi (3.8 vs 2.1 Å) and so will measure more data, covering a wider range of *d*-spacing, in a single orientation of the crystal sample. From the Ewald sphere construction:

$$n = \frac{4}{3}\pi\left(\frac{1}{\lambda}\right)^3 V$$

where n is the number of reflections and V is the unit cell volume, a 1–4.8 Å wavelength range (LMX) versus 2–4 Å (MaNDi) gives almost an order of magnitude more reflections that are theoretically measurable. This is made possible, predominantly by the shorter wavelengths. The longer wavelengths give access to longer *d*-spacing reflections, from Bragg's law:

$$d_{\max} = \frac{\lambda_{\max}}{2\sin\theta}$$

at a given forward scattering diffraction angle, e.g. $2\theta = 30°$, then $\lambda_{\max} = 4$ Å gives $d = 7.7$ Å (MaNDi) and $\lambda_{\max} = 4.66$ Å gives $d = 9.0$ Å (LMX) which is advantageous for large-unit-cell systems.

The samples measured on LMX will typically be small, and have large unit cells. Measurement times are necessarily longer than for smaller-cell compounds due the weakly-scattering nature of the materials, but this represents an entirely new capability gain for ISIS – there is currently zero capability for measuring diffraction patterns from macromolecular materials. Longer count times are typical for this science area – a summary Table (8.1) in the Appendix shows that other major biological crystallography instruments require long measurement times. In Europe, the quasi-Laue LADI-III (ILL) instrument has reported anything up to 30 days to measure a sample, and the monochromatic BIODIFF (MLZ) instrument, up to 22 days. However, measurement times can also be significantly shorter where large sample volumes are available (see Table 8.1).

Probable measurement time for LMX is difficult to estimate from simulations and, experimentally, it will be highly sample-dependent (unit cell size, scattering power, symmetry, crystallinity), since the major source of background will originate from incoherent scatter in hydrogen-rich samples. These factors will all dictate measurement counting times. A comparison with MaNDi, over a 2-4 Å waveband is the most straightforward. MaNDi views a decoupled hydrogen moderator at the SNS and this provides ca. 2–2.5× increase in flux relative to the refurbished hydrogen moderator at ISIS TS1. However, the relatively sharper time structure on MaNDi means a larger proportion of beam intensity for LMX would be located in the peak tail, effectively resulting in a ca. 4× difference. Figure 6.1 illustrates the flux differences between the two instruments.

Taken in isolation, this represents a factor of four difference in measurement time. However, the mitigation against this is to reduce the number of orientations over which the crystal must be sampled in order to obtain a complete dataset. This is achieved by measuring diffraction over a larger solid angle. The detector array on MaNDi covers 4.1 sr and though the exact coverage on LMX will be

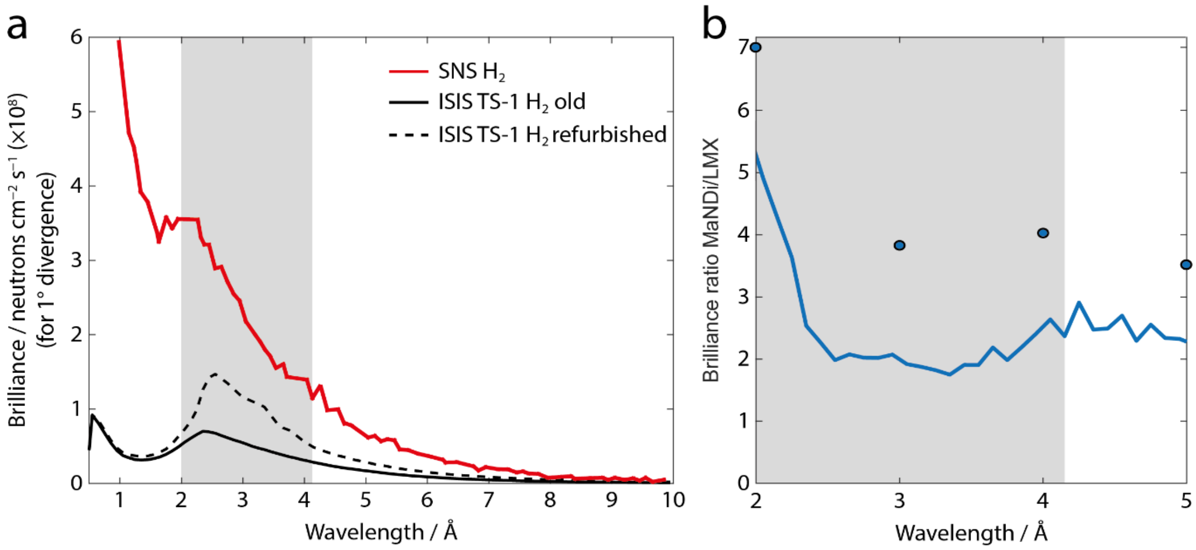

Figure 6.1. a) Brilliance comparison between SNS and ISIS H_2 moderators, before and after refurbishment. The grey region indicated the 2–4 Å waveband; the region over which the MaNDi instrument measures. **b)** Brilliance ratio between MaNDi and refurbished ISIS H_2 moderators – the solid line represents a division of the plots shown in a). The dots take into account the proportion of neutrons present in the principal peak/peak tail. This leads to ca. 4× difference in useful neutron flux.

informed during the next phase when design effort becomes available, the anticipated coverage with WSF detectors is close to 9 sr – over double that of MaNDi. Taking flux and detector coverage differences together, this should mean data collection times on LMX are nominally twice as long as MaNDi, meaning the former outperforms the latter on a per-power-unit basis.

Typical measurement examples from MaNDi, on samples that would fall within the capability of LMX are as follows:

Example 1: NaK2K mutant protein - hydrogenated
Reference: PS Langan *et al*, *Acta Crystallogr.*, 2019, **F75**, 435–438
Crystal volume: 0.3 mm^3
Unit-cell parameters: $a = b = 67.86$ Å, $c = 92.03$ Å, $\alpha = \beta = \gamma = 90°$
Unit-cell volume: 423,796 Å^3
Space group: *I*4
d_{min}: 3.6 Å
$\lambda_{\min}$, $\lambda_{\max}$: 2.00, 4.16 Å
Temperature: 293 K
Crystal orientations: 8
Measurement time: 7 days (21 hours per orientation)

Example 2: Z-DNA hexamer d(CGCGCG) – partially deuterated
Reference: JM Harp *et al*, *Acta Crystallogr.*, 2018, **F74**, 603–609
Crystal volume: 0.25 mm^3
Unit-cell parameters: $a = 17.89$ Å, $b = 30.77$ Å, $c = 43.71$ Å, $\alpha = \beta = \gamma = 90°$
Unit-cell volume: 24,061 Å^3
Space group: $P2_12_12_1$
$d_{\min}$: 1.7 Å
$\lambda_{\min}$, $\lambda_{\max}$: 2.00, 4.16 Å
Temperature: 100 K
Crystal orientations: 12
Measurement time: <2 days (3.5 hours per orientation)

The first example represents a typical hydrogenated protein, measured at ambient temperature, and the second has a smaller unit cell, partial deuteration, and is measured at a low temperature. Given the approximate twofold difference in measurement time that is anticipated on LMX, these would likely take 14 and 4 days, respectively. The second sample, having a smaller unit cell size, bears more similarity to the chemical samples that will be measured on the LMX user programme and so gives an indication of measurement timescale.

With respect to performance against other macromolecular European instruments – LADI-III, DALI, and BIODIFF, LMX will be a lower flux instrument – ca. 10× less than the quasi-Laue LADI-III instrument. However, LMX will benefit from the advantages of the time-of-flight technique. This allows background scattering (significant for biological crystals) to be spread over several time channels, offering far improved signal-to-noise. This same advantage will also allow spatially-overlapped reflections to be time-resolved. Greater detector coverage on LMX will lead to a reduction in collection time as fewer orientations of the crystal will be required to obtain a complete data set. The wider wavelength range on LMX will also assist with this allowing an increased number of reflections to be accessed over a greater range of scattering angles relative to the monochromatic/quasi-Laue instruments.

An approximate time comparison between LMX and the LADI-III instrument can be made by contrasting the refinement statistics in Table 6.1, taken from F. Manzoni et al, *Acta Crystallogr.*, (2016), **D72**, 1194–1202. The main difference between the three measurements is the crystal size used in each and, consequently, the variable measurement time required for each. Taking averages of these for the LADI-III measurements gives a crystal size of 1.075 mm^3 and a 13.5 day experiment. This almost directly corresponds to the MaNDi measurement (1.0 mm^3, 14 days). Therefore experiments on LMX should take approximately twice as those on LADI-III, despite the ca. 10× reduction in flux.

Instrument	**LADI-III**	**LADI-III**	**MaNDi**
Resolution / Å	30.0–1.9 (2.0–1.9)	28.0–1.7 (1.8–1.7)	19.0–1.6 (1.7–1.6)
Unit cell / Å	a = 37.3, b = 58.5, c = 63.8	a = 37.2, b = 58.6, c = 64.1	a = 37.3, b = 58.4, c = 64.0
$R_{\mathrm{merge}}(I)$ %	14.7 (19.7)	16.2 (20.8)	15.5 (20.7)
$R_{\mathrm{p,i,m}}(I)$ %	5.3 (11.1)	4.4 (7.6)	6.6 (15.0)
Mean I/σ	11.8 (6.2)	12.4 (7.0)	12.2 (2.4)
Completeness %	86.6 (72.4)	87.1 (66.5)	81.3 (54.6)
Unique reflections	9844 (1177)	13741 (1490)	15485 (1022)
Multiplicity	6.3 (3.6)	10.0 (4.9)	4.4 (1.7)
Time / days	21	6	14
Crystal size / mm^3	0.35	1.8	1.0

Table 6.1. Refinement statistics for three instances of lactose (galectin-3C, $P2_12_12_1$) measured on LADI-III and MaNDi. Values in parentheses correspond to the outermost resolution shell.

6.2. Test measurement on WISH

ISIS does not currently have a single-crystal diffractometer that has the level of flux that LMX would have, which would exploit both the brilliance gain in the refurbished TS1 H_2 moderator, as well as the TS1 repetition rate. The closest comparison is with the existing WISH diffractometer, which is located on TS2 and views a solid CH_4 moderator. The respective performances of these two moderators was assessed in Section 4.3.

A test measurement was made on the WISH instrument of a rubredoxin protein crystal ($P2_12_12_1$, a = 34.44, b = 35.14, c = 43.78 Å), selected due to this being a reliably-known sample to the extent that it is used to calibrate dedicated protein diffractometers (LADI-III). Additionally, the sample represents an excellent compromise between the materials that LMX would measure – between the dimensions of the smallest 'chemical' samples and the largest proteins.

A perdeuterated rubredoxin crystal was sealed in a glass capillary, keeping it immersed in its mother liquor to avoid degradation of the sample. The crystal was collected in six orientations to improve data completeness owing to the low solid angle coverage of WISH (relative to LMX), having detectors in the equatorial scattering plane only. 200 µA of neutrons were collected in each run, taking ca. 5 hours in each orientation – i.e. a total collection time of 30 hours.

Taking a single run as being representative of the others, following data integration, a total of 767 reflections with $I/\sigma > 3$ are measured in one orientation of the crystal. 714 of these have $I/\sigma > 5$, and 489 have $I/\sigma > 10$. Note that additional reflections are identified, but the current form of the integration routines uses $I/\sigma > 3$ as a cut-off threshold for *hkl* output. WISH uses a wider wavelength range than LMX will (ca. 1–10 vs 1–5 Å), and so filtering the reflections to λ = 1–5 Å leaves 557 reflections with $I/\sigma > 3$, 513 with $I/\sigma > 5$ and 332 with $I/\sigma > 10$.

Figure 6.2 shows a visual summary of the measurements. Panel **a)** shows select reflections, their measurements conditions and profiles, and their I/σ values. Each column from left-to-right shows reflections measured in forward scattering, near-transverse, and back scattering geometries. Panel **b)** simply shows a collection of reflection profiles across the detector panel using λ = 1–10 and 1–5 Å on the left and right respectively. Note the vertical black lines are artefacts generated by the rendering by the Mantid software. The WISH instrument uses large axial beam divergence, so all reflections appear vertically elongated. Panel **c)** shows a slice through reciprocal space with measured reflections for the (*h*2*l*) layer.

Though there are clear differences between the characteristics of the WISH and LMX instruments, a combination of this measurement and the simulations showing the relative gains in TS1 H_2 moderator brilliance/source repetition rate (Section 4.3) demonstrates the feasibility of large-molecule single-crystal measurement on LMX.

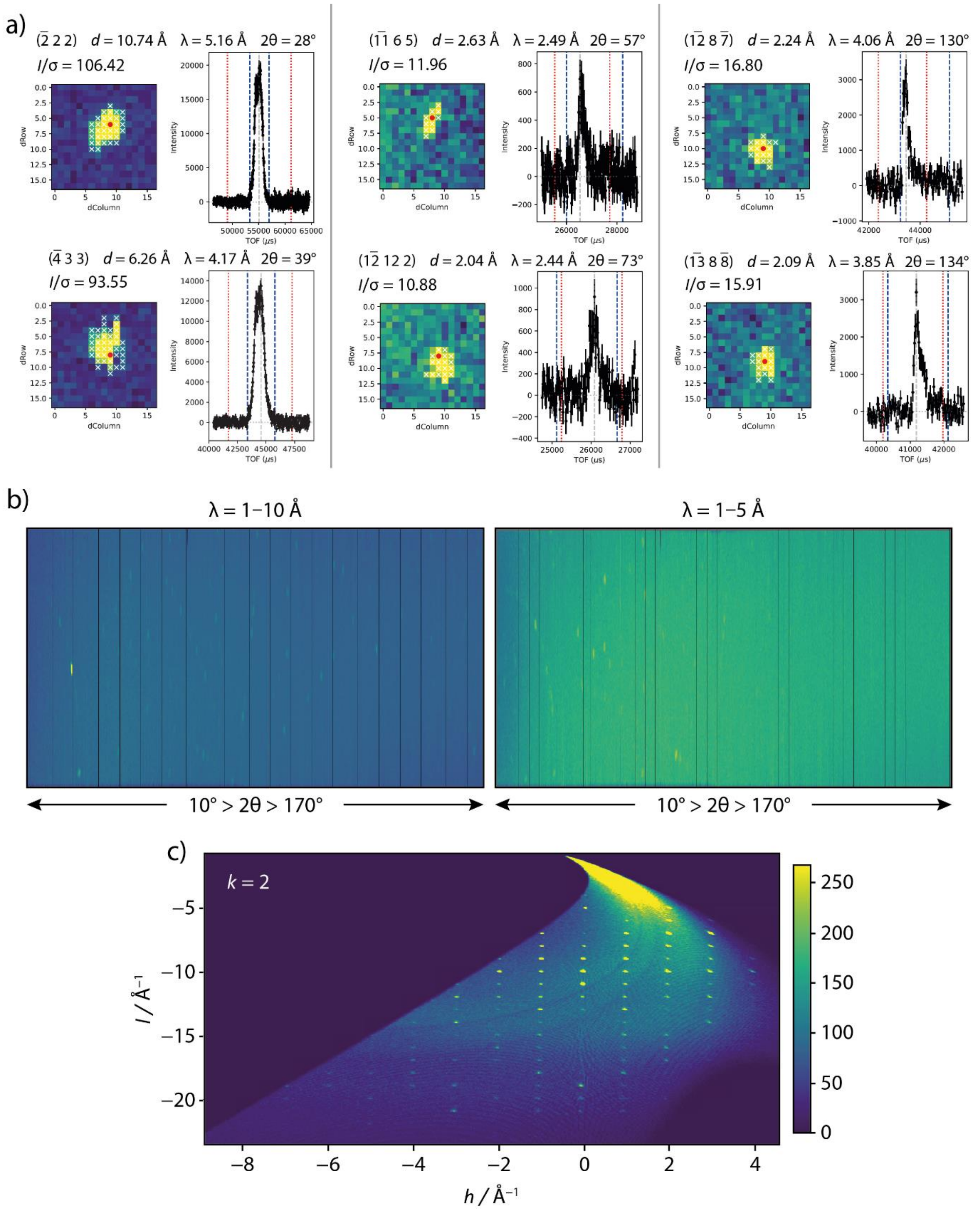

Figure 6.2. a) Select (hkl) reflections showing spatial and ToF profile. Measurement conditions and statistics are indicated by each reflection. Columns left-to-right show increasing 2θ diffraction angle. **b)** Distribution of Bragg peaks on one WISH detector panel, shown for the full wavelength range (left) and 1–5 Å (right). The vertical black lines are graphical artefacts. **c)** Reciprocal space slice showing the (*h*2*l*) layer.

6.3. Instrument complementarity

In terms of performance with respect to capability, LMX complements the existing, and anticipated, instruments at ISIS, as well as those covering the wider European landscape.

At ISIS, the only dedicated single-crystal instrument is SXD, which is optimised to measure using short-wavelength neutrons, delivering on its remit to study small-molecule crystal structures. It lacks the time resolution, and wavelength range to measure larger unit cells that are typical of supramolecular/macromolecular crystal structures. LMX will offer the capability to measure materials with unit cells larger than SXD can measure (ca. 40 Å), up to (and possibly beyond) the 120 Å cell edge for which it has been optimised. This spans a wide range of chemical and biological materials.

LMX will also complement the long *d*-spacing measurement capability offered by the WISH (and WISH-II) instrument as the science remits will deliver biological/chemical crystallography, and magnetic structure characterisation, respectively. Moreover, the increased flux of the TS1 hydrogen moderator over the 2-3 Å region will enable LMX to measure what will typically be very small, weakly-diffracting samples more rapidly than would be possible on WISH/WISH-II at these wavelengths.

The upcoming closure of the ILL will reduce European single-crystal measurement capacity, with the loss of several instruments; LMX will provide capacity for users of the D19, LADI-III, and DALI instruments. Additional European capability will be added in the form of the NMX instrument at the ESS, once it is operational. However it will be optimised to measure substantially larger unit cell sizes (ca. 300 Å) than LMX, meaning that the two instruments will complement each other, rather than compete. While NMX will offer a ca. 500× gain in neutron flux (across 1.8–3.55 Å, with ±0.2° divergence), in order to measure very large unit cells from small crystal volumes, LMX will possess ca. 8× greater time resolution – again to the benefit of improved signal-to-noise statistics.

7) Technical risks

LMX has a simple design and, overall, should present limited technical risk. There are no new, untested, components being included – it does not require any new developments. It is simply comprised of an elliptical guide, a t_0 chopper, two single-disc frame-overlap choppers, two jaw sets, and detectors completely surrounding the sample position. Design effort is required to fully evaluate the proposed instrument concept.

The newest items will be the double-layer WSF detectors – at time of writing, the double-layer variants have been tested on SXD and have been shown to be effective, attaining their anticipated performance. These detectors span multiple projects and are not specific to the LMX. The effectiveness of electronic pixel rebinning is currently being investigated on SXD. Should rebinning not prove possible, then the mitigation against this risk would be to move detector distances to longer L_2, allowing for larger physical pixel sizes.

The instrument is designed to have a uniform beam divergence, which can be reduced via moveable jaws, suitable for measuring small samples with large unit cells, requiring careful alignment of the beam, oscillating radial collimator (ORC), and sample. In the worst case scenario, the ORC will be entirely removable. However, other instruments worldwide, e.g. SENJU measure very small samples (0.5 mm^3) with a removable ORC, so this is not anticipated to be a serious problem.

Appropriate sample preparation (deuteration/crystal growth) will be important for the instrument user programme. Though ISIS has significant in-house expertise with sample deuteration, this does not currently extend to biological crystals. Expanding this facility is recognised to be an important aspect of developing the Life-Science and Healthcare focus area within the ISIS Science Strategy – i.e. it has relevance beyond just LMX. We are currently establishing a cross-campus network working towards developing this capability, and are engaged in discussions with other facilities around the world, including the European Molecular Biology Lab and ILL (Grenoble, France), the ESS (Lund, Sweden), and the SNS (Tennessee, USA).

The operational (construction) risk lies in resourcing and manpower available, which cannot be mitigated against in the LMX design. However, this is a risk that is applicable to all instruments across the Endeavour programme.

8) Appendix

8.1 Internal review recommendations and point-by-point response summary

An overview of the changes that have been made are noted after each recommendation below. The detailed simulations/analysis addressing each of these are provided in Sections 4 and 5.

***1) Moderator*.**

Macromolecular diffraction is a rate limited technique, so the team have chosen the coupled hydrogen moderator on TS1, as the brightest ISIS source in their needed wavelength range. This is likely to be the best moderator, but first impressions are not always correct. Half the flux of the hydrogen moderator is in the very long tail, itself acting as an additional source of background. Viewing the solid methane moderator would make use of the higher peak brightness as opposed to average brightness of that moderator compared to the TS1 hydrogen one [Goran's report]. If LMX was on the methane moderator of TS2 it could sit further out (near 40m) which would lower backgrounds by a factor of 2 (TS2 also more quiet generally) and it would still have a broader bandwidth, plus it has very little tail compared to the hydrogen. Alternatively, if accessing long d-spacings is relevant to the science case, it could still be a ~20m instrument with a larger bandwidth, greatly reducing the need for rotations to access long d-spacings that would only be accessible at very low angles. It should also be noted that resolution can help bring peaks out from background, which is anticipated to be significant on LMX due to the nature of the samples studied with large incoherent contribution. Perhaps these factors could tip the balance in favor of methane. Simulations would be needed taking into account the large incoherent backgrounds from the hydrogenous samples (and considering the mother liquid). This is relatively easy in McStas using an incoherent sample in parallel to the coherent crystal.

The panel would highly recommend the team perform a test experiment on WISH, using a well-known and understood biological sample. WISH views the methane, is at 40m, can control its incoming divergence, and has very low backgrounds with an effective pixel size of 2mm @ 500mm radius. Although it does not have the detector coverage of LMX, it will be a great test of the sort of detector count rate and signal/noise one can expect at ISIS. Scaling these results will also give us a good idea of what to expect on the hydrogen moderator.

Response:

Additional simulations have now been performed, contrasting the relative brilliance of the TS1 hydrogen and TS2 methane moderators. As a part of this section, the effects of incoherent scattering have been simulated to assess the level at which one moderator might outperform the other. The simulations indicate that the hydrogen moderator is superior for the case of weakly-scattering materials/elucidating Bragg reflections in the presence of large background levels.

The possibility of performing a measurement on WISH was considered however it would only show whether a given (known) sample could be measured with the methane moderator or not. We would still be dependent on simulations to indicate whether it is more advantageous to use a hydrogen moderator – the simulations detailed in Section 4 already show this to be the case.

***2) Choppers*.**

T zero *The review team agree that a T zero is likely to be unnecessary due to the low power source, but to leave a space just in case. We would encourage the team to calculate the potential sweep time of the chopper at its current position to make sure it does not obstruct wanted neutrons at short wavelengths. Also, when possible (if you can get an engineer) that there is the physical space at this position.*

Bandwidth choppers *We recommend putting the first disk chopper at 6 m instead of the current 6.5 m (swapping its position with the T zero) and the second at 9 m instead of 10.05 m. This cuts out the unwanted slow neutrons from previous frames at around 14 Angtroms. You still get unwanted higher wavelength neutrons around 25 angstroms but they could easily be removed by putting a frame overlap mirror in the final section between the two sets of slits. We recommend simulating the frame overlap mirror at this position.*

Each disk chopper is around £100k and LMX plans to use 4 disks (2 sets of counter rotating) with disk radius of around 30 cm. You could possibly use (need to check space with neighboring instruments) much larger 60 cm radius disks (as used on WISH and LET) and get the same cut times as present with just 2 disks.

Response:

The frame overlap choppers are now located at the recommended positions. Simulations that include a frame overlap mirror between the two final set of slits show that the wavelength band at ca. 26–31 Å is reduced to a negligible intensity.

As a consequence of other changes to the instrument – specifically use of an elliptical guide that accepts a smaller beam size – the design now uses two, standard-dimension, single-disc frame overlap choppers, with no degradation in cut time. Reduced wavelength-divergence structuring is now seen in the guide, partly due to the reduced gap size accommodating the second chopper.

Moreover, the reduced beam size means a smaller blocking blade is required for any future t_0 chopper. The calculated total sweep time is 6.5×10^{-4} s, so neutrons taking 3.25×10^{-4} s to reach 6 m after t = 0 s will be unmeasurable. This means that the 0–0.22 Å range of wavelengths cannot be accessed, however this is safely below the desired wavelength band (ca. 1–5 Å).

***3) Guides**.*

The suggested design is very simple, cheap and effective with almost perfect Brilliance transfer within the wanted phase space. To save some money we advise grading the 'm' values, highest 'm' nearest the sample to lower m values nearest the moderator. (Rob Bewley has some code to do this grading). In the TDD it would be informative to show the guide simulation results as a figure of merit (FOM) scan, where the FOM in this case is probably the integral of the BT over the wanted wavelength range.

A possibility brought up in the review was to make a pinhole secondary source outside the biological wall and then using an elliptical guide to focus this onto the sample. If it's feasible the advantages would be lower backgrounds (as you are only transporting the wanted phase space down the guide) and much faster chop times at the bandwidth and T zero choppers as the beam dimension is much smaller. (possibly the extra cost of the guide is balanced with reduced dimension of choppers and it will be much easier for space constraints)

Response:

Simulations indicate an elliptical guide is a more desirable option for the instrument, due to the reduction in unwanted phase space being transported – the guide-illuminated area outside the sample volume is significantly reduced. However use of a secondary pinhole source led to an inhomogeneous beam with respect to divergence, so a direct view of the moderator has been maintained.

The smaller guide opening means that faster chop times are possible (single-disc choppers are now being used) and there is a reduced direct view of the moderator fact, helping lower any gamma radiation. The guide optimisation is now shown using a FOM scan.

4) Detectors.

The TDD did not give any details of what the detector arrangement would look like. While it is appreciated that in detailed engineering this could change it is still important that your vision for what you want is presented. We would encourage the LMX team to look at the WISH II design. It is a simple almost gap free design, utilizing 16 square panels and 8 triangular panels of WSF. An even simpler design is the cylindrical design (shown by Dom) composed of just square panels. This shape is also very compatible with the use of a radial collimator. However, L2 varies more (not necessarily an issue) and neutrons will hit the cylinder ends at oblique angles. Whether this causes problems with neutron positioning and indeed signal to noise as the signal is spread over a larger area would need further investigation.

Detector L2 and pixel size. *The examples given in the TDD were not convincing as the large mosaic spread of the sample dominated all the results and made the pixel size and L2 almost irrelevant. Choose your best crystal mosaic (0.1 degrees was mentioned in the review) and match this with your incoming beam divergence, then simulate as a function of L2 and pixel size. Ideally, the pixel size should be smaller than your sample size (with electronic positioning), so no bigger than 1 mm which at 500 mm radius is about 0.1 degrees, matching the best resolution conditions.*

Response:

We find the cylindrical arrangement to be the better option in terms of design simplicity, solid angle coverage, and compatibility with the collimator geometry – this is shown schematically in Section 5. Simulated reflection profiles at the upper/lowermost edges of the detector indicate that there should not be any issues with oblique angles (Section 4), which means it would be preferable to either the WISH-II design, or previously-proposed spherical-arrangement. The detector L_2 and pixel size simulations have now been repeated using minimal mosaic spread and small angular divergence (Section 4). Determining the final detector layout is dependent on engineering resource.

Additional point raised

The instrument as designed will fulfil the key instrument drivers as presented in the TDD and thus should fulfil the science case. The simulations presented show that the spatial and time resolution of LMX would be capable of resolving the structure of macromolecular crystals up to the designed maximum of about 120 Å unit cell length. What was not so clear to the reviewers (none are experts in this field) was if the resolution was good enough for everything they wanted to do with chemical crystal analysis, in particular if there was interest in phase transitions where high resolutions are often needed. Indeed, the design has been optimised with maximum flux with just enough resolution to separate peaks via fitting.

Response:

The remit of LMX is to perform high-quality structural characterisation from 3D data, i.e. determination of atomic connectivity while benefiting from the ability to measure light atom species with neutrons. This is not the same as measuring phase transitions. For this reason, the LMX Science Case does not mention the study of phase transitions.

This point really refers to a specific category of phase transformation: 'continuous', symmetry-related transitions, which are prevalent in materials that exhibit concerted rotations in polyhedra, e.g. perovskites. This can lead to (sometimes subtle) reflection splitting, corresponding to symmetry-lowering, which are better studied on (high-resolution) powder diffractometers.

So-called 'reconstructive' transitions form another widely-encountered type of transformation, where the changes are more pronounced, e.g. changes in molecular packing, which LMX will be sensitive to. Continuous transitions are rarely observed in organic/organometallic molecular crystals, or biological structures, which will likely comprise the majority of the LMX science programme.

However, LMX will make use of non-ambient sample environments (pressure, temperature, light) which may well induce phase transitions. It would be the expectation that if the transition were very subtle, it would be studied on a different instrument, but LMX will still offer some capability to study transitions. The Key Drivers mean the instrument resolution has been optimised around d-spacing = 2 Å of a 120 Å cubic unit cell. This is a cell dimension that will almost certainly only be seen for biological materials. 'Chemical' materials will be smaller – an identical resolution ($\Delta d/d = 0.0165$) is achievable for $d = 1$ Å with a 60 Å cell edge. Moreover, the instrument likely exceeds this resolution although this is not straightforward to quantify – see Section 4.4.

8.2 Peak fitting parameters for the refurbished hydrogen moderator

In Mantid, a time-of-flight diffraction peak can typically be fitted with the back-to-back exponential function, which can be expressed as:

$$I\,\frac{\alpha\beta}{2(\alpha+\beta)}\left\{exp\left[\frac{\alpha\left(\alpha\sigma^2+2\{x-x_0\}\right)}{2}\right]erfc\left[\frac{\alpha\sigma^2+(x-x_0)}{\sigma\sqrt{2}}\right]\right\}+\left\{exp\left[\frac{\beta\left(\beta\sigma^2-2\{x-x_0\}\right)}{2}\right]erfc\left[\frac{\left(\beta\sigma^2-(x-x_0)\right)}{\sigma\sqrt{2}}\right]\right\},$$

where x_0 is the peak position, α and β are the exponential constants for the rising, and decaying, components of the peak, respectively, and σ the standard deviation of the Gaussian contribution.

A single peak was simulated across a range of wavelengths at a fixed scattering angle (2θ = 142.5°). To fit the principal peak (hereafter ‘peak A’) and the secondary peak arising from the water pre-moderator (‘peak B’), a series of fits were performed using two independent fits to the contributing parts of the overall diffraction peak. In all cases, α was found to be invariant with wavelength/ToF and was held fixed to 0.4. β and σ showed a linear trend as a function of peak A position in ToF, shown in Figure 8.1. Additionally, there is a linear relationship between the positions of peak A and B, and the intensity ratio between the two can be approximated with a fourth-order polynomial.

The peak fits shown in Figures 4.3 and 4.4 were performed by constraining all parameters, including peak positions and intensities, to the relationships shown in Figure 8.1. The only freely-refining parameters were X_0 for peak A, and its intensity.

Though peak fitting will be complicated by the fact that the peak shape is affected by both wavelength and scattering angle, the preliminary work here demonstrates that this is possible.

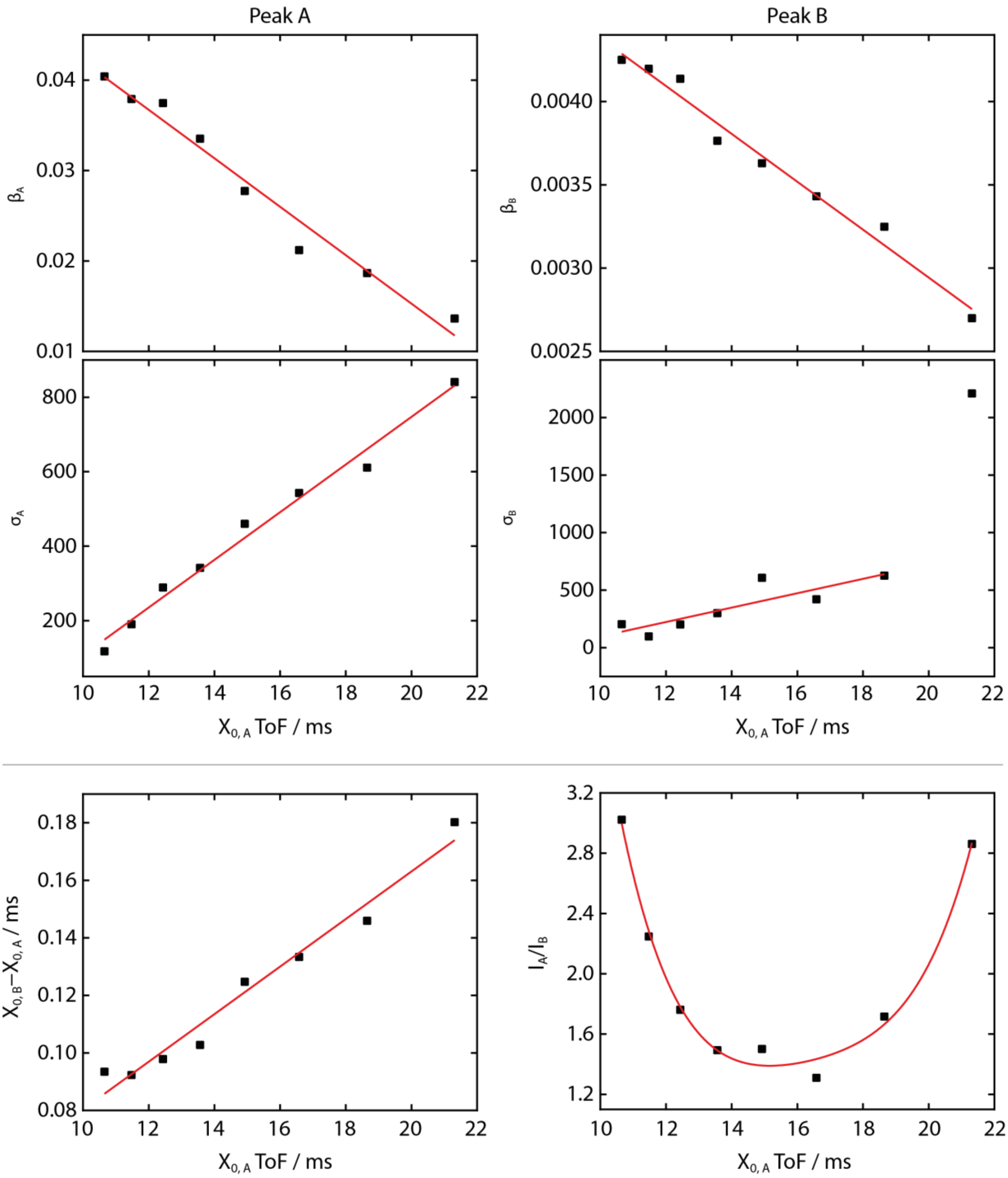

Figure 8.1. Peak parameter fits shown as a function of principal peak (‘A’) position, as well as relationships between peak position and intensity between peaks ‘A’ and ‘B’. Any clearly-outlying points were omitted from the fits.

8.3 Effect of reducing instrument length on time resolution

The effect of reducing the primary flight path length to 16 m means that the λ = 1–5 Å neutrons can be measured within a single frame, i.e. without spanning the prompt pulse. However, this necessarily results in reduced time resolution, illustrated in Figure 8.2. Though the (0 60 0) and (0 61 0) reflections are evident across all measurement conditions, it becomes increasingly difficult to resolve the two reflections with a shorter instrument.

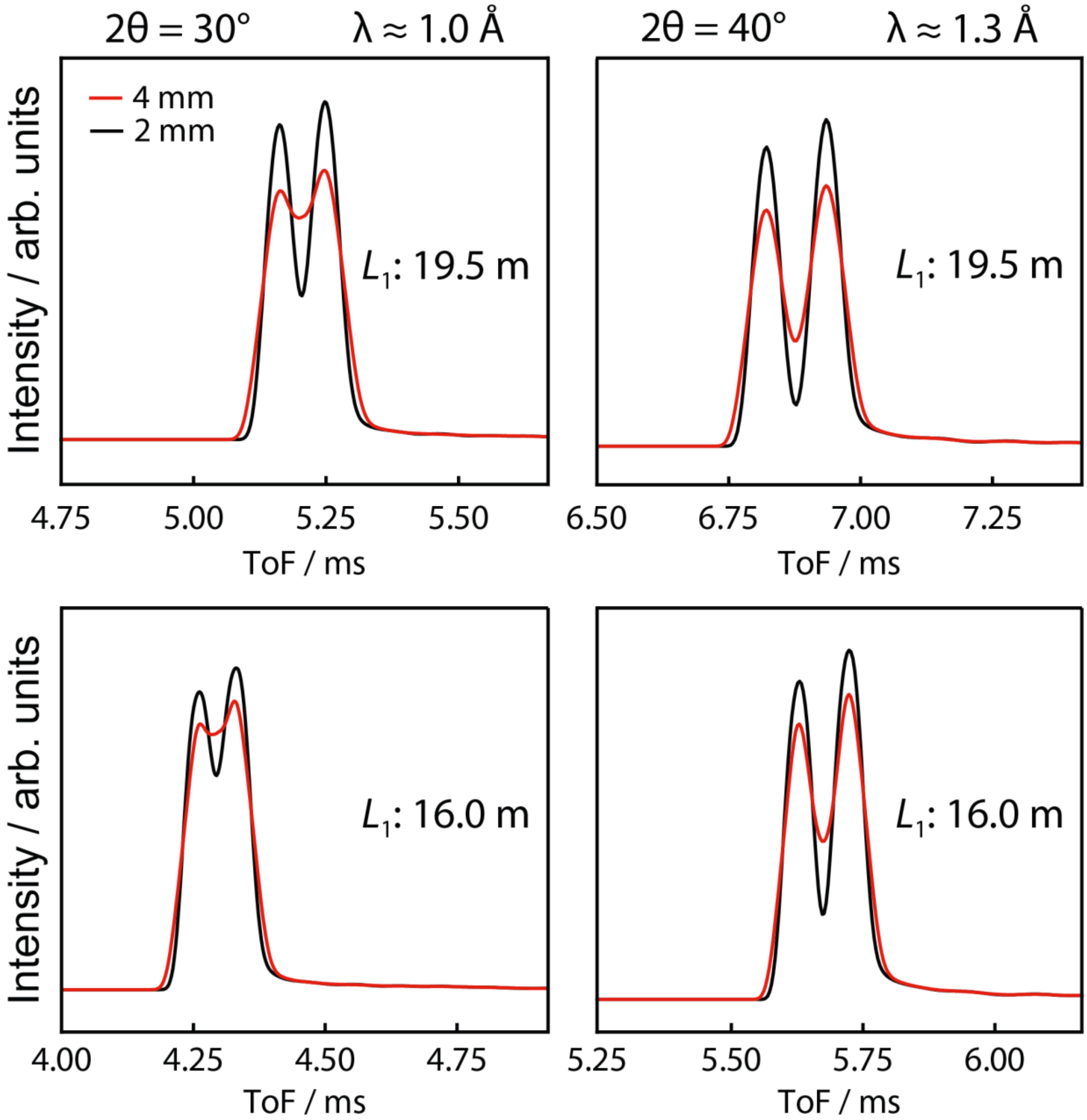

Figure 8.2. Time-of-flight resolution of the (0 60 0) and (0 61 0) reflections using a 19.5 m primary flight path (top row) and 16 m (bottom row). The left column corresponds to scattering at 2θ = 30° (λ ≈ 1.0 Å) and the right column 2θ = 40° (λ ≈ 1.3 Å). Detector pixel sizes of 4 mm and 2 mm are shown for each measurement condition.

8.4. Effect of gravity on beam transport

All McStas simulations accounted for the effects of gravity, using $G = 9.8\ \text{ms}^{-1}$; no clear effect was seen over the 1−5 Å waveband. To ensure that gravitational effects were being applied, longer wavelengths were simulated using a uniform-intensity source, *m*-coating = 5, and the full beam divergence range ±0.4°. The results are plotted below, showing clearly that brilliance transfer decreases with increased wavelength – it falls to ca. 90% for 26–31 Å (contaminant wavelength band discussed in Section 5.3), eventually falling to 0% at very long wavelengths (70−75 Å). In all cases, brilliance transfer remains at ca. 100% when gravity is not applied.

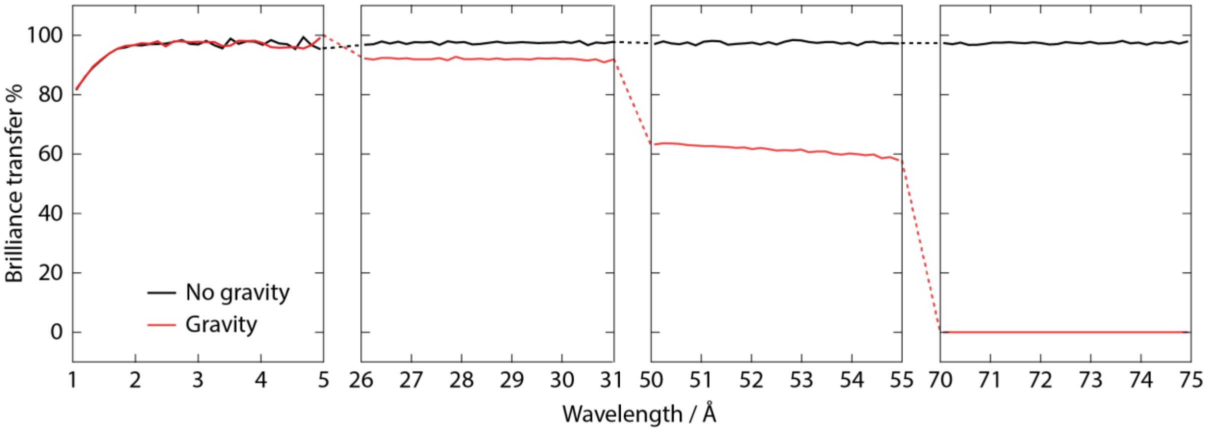

Figure 8.3. Brilliance transfer as a function of wavelength and simulation of gravitational effects. 1–5 Å is the desired measurement region. 26–31 Å covers the region over which one of the contaminant wavebands reaches the sample. The longer wavelengths at 50–55 and 70–75 Å, covering very long wavelengths, demonstrate the complete fall-off in neutron transport.

8.5. Measurement details of macromolecular crystal structures

PDB code	$d_{\min}$ / Å	Crystal vol. / mm^3	Unit cell vol. / Å^3	Asym. unit vol. / Å^3	Space group	Time / days	Instrument
4C3Q	2.2	0.95	452000	75300	$P3_221$	7	BIODIFF
4BD1	2	2.7	452000	75300	$P3_221$	7	BIODIFF
4Q49	1.8	2	125000	62500	$P2_1$	8	BIODIFF
4CVJ	2.5	0.7	428000	107000	$P2_12_12_1$	22	BIODIFF
4AR4	1.38	2	51000	12750	$P2_12_12_1$	3	D19
3KCJ	1.8	28	984000	123000	$I222$	6	D19
4AR3	1.05	6.9	51000	12750	$P2_12_12_1$	8	D19
4PVN	2.3	3.4	248000	62000	$P2_12_12$	10	D19
4QDW	1.8	10	984000	123000	$I222$	14	D19
4DVO	2	50	984000	123000	$I222$	14	D19
3KCL	2	50	984000	123000	$I222$	14	D19
4QCD	1.93	2.7	299000	74750	$P2_12_12$	9	iBIX
3U2J	2	2.5	248000	62000	$P2_12_12$	30	iBIX
4K9F	1.75	0.7	51000	12750	$P2_12_12_1$	3	IMAGINE
4PDJ	2	3.6	155000	38750	$P2_12_12_1$	17	IMAGINE
3RZT	1.75	3.2	51000	12750	$P2_12_12_1$	0.5	LADI-III
3RZ6	1.75	3.9	51000	12750	$P2_12_12_1$	1.5	LADI-III
3SS2	1.75	3.9	51000	12750	$P2_12_12_1$	2	LADI-III
3KYY	1.66	4.1	51000	12750	$P2_12_12_1$	3	LADI-III
4PVM	2	3.4	248000	62000	$P2_12_12$	5	LADI-III
3RYG	1.75	3.9	51000	12750	$P2_12_12_1$	5	LADI-III
3KYX	1.68	3.9	51000	12750	$P2_12_12_1$	5	LADI-III
4N3M	1.9	4	815000	101870	$I222$	6	LADI-III
2XQZ	2.1	5	452000	75300	$P3_221$	6	LADI-III
AxCytCp	2.1	1.5	431000	35900	$P6_522$	10	LADI-III
2WYX	2.1	8.75	452000	75300	$P3_221$	12	LADI-III
AcNiR	2.3	0.3	893000	74400	$P2_13$	15	LADI-III
4JEC	2	0.2	240000	60000	$P2_12_12$	17	LADI-III
4QXK	2.2	0.95	249000	31120	$P4_12_12$	17	LADI-III
4CVI	2.4	1	428000	107000	$P2_12_12_1$	18	LADI-III
3QFS	1.85	0.13	59000	14750	$P2_12_12_1$	21	LADI-III
3Q3L	2.5	5	1141000	285250	$C2$	21	LADI-III
3R98	2.4	1	428000	107000	$P2_12_12_1$	25	LADI-III
3R99	2.4	1	428000	107000	$P2_12_12_1$	25	LADI-III
4N9M	2.3	1	815000	101870	$I222$	25	LADI-III
4NY6	1.85	0.23	59000	14750	$P2_12_12_1$	30	LADI-III
3QZA	2	9.4	984000	123000	$I222$	14	PCS
4QDP	2	10	984000	123000	$I222$	14	PCS
3KCO	1.8	50	984000	123000	$I222$	14	PCS
3TMJ	2	1.7	125000	62500	$P2_1$	20	PCS
3L45	1.8	2	45000	22500	$P2_1$	21	PCS
4GOC	2	2	125000	62500	$P2_1$	22	PCS
4YOJ	2	2	125000	62500	$P2_1$	22	PCS
4FC1	1.1	4	18000	9000	$P2_1$	22	PCS
3KMF	2	20	289000	144500	$P2_1$	23	PCS
3QBA	1.4	0.7	24000	6000	$P2_12_12_1$	25	PCS
3KKX	2	1.2	125000	62500	$P2_1$	55	PCS

Table 8.1. Measurement details of joint X-ray/neutron structures deposited in the PDB between 2010 and 2015. Adapted from MP Blakeley *et al*, *IUCrJ*, 2015, **2**, 464–474.

8.6. Previous (pre-review) design details for choppers

50 Hz, 0.35 m radius, double disc choppers at 6.51 m (opening 133.81°) and 10.05 m (opening 190.70°).

Sufficient space for a t_0 chopper (0.5 m) has been incorporated into the baseline design, beyond the outer wall of the biological shielding.

In order to deliver a wide waveband $L_1 + L_2 = 20$ m, while minimising contamination of frames with long wavelength neutrons, chopper positioning was guided by a phase space diagram – see Figure 8.4. The first of these was located at 6.51 m, allowing space for a t_0 chopper to precede it. The Figure shows the wavelength and time phase space at the moderator; each band indicates successive chopper openings. These coincide for the first opening of both choppers, but are ideally staggered beyond the desired wavelength range. However, overlaps occur quite frequently at shorter wavelengths, which can only be suppressed by either i) moving the first chopper < 6 m (i.e. within the biological shielding – expensive/not possible), ii) including a third chopper (reducing beam divergence homogeneity), or iii) minor waveband reduction (simplest option). Given that the phase space diagram does not allow for opening/closing times of the choppers, option iii) is the most sensible as only a small reduction to 3.8 Å is required. Then by adjusting the position of the second chopper (to 9.8 m), the first significant (and undesired) overlap does not occur until ca. 30 Å.

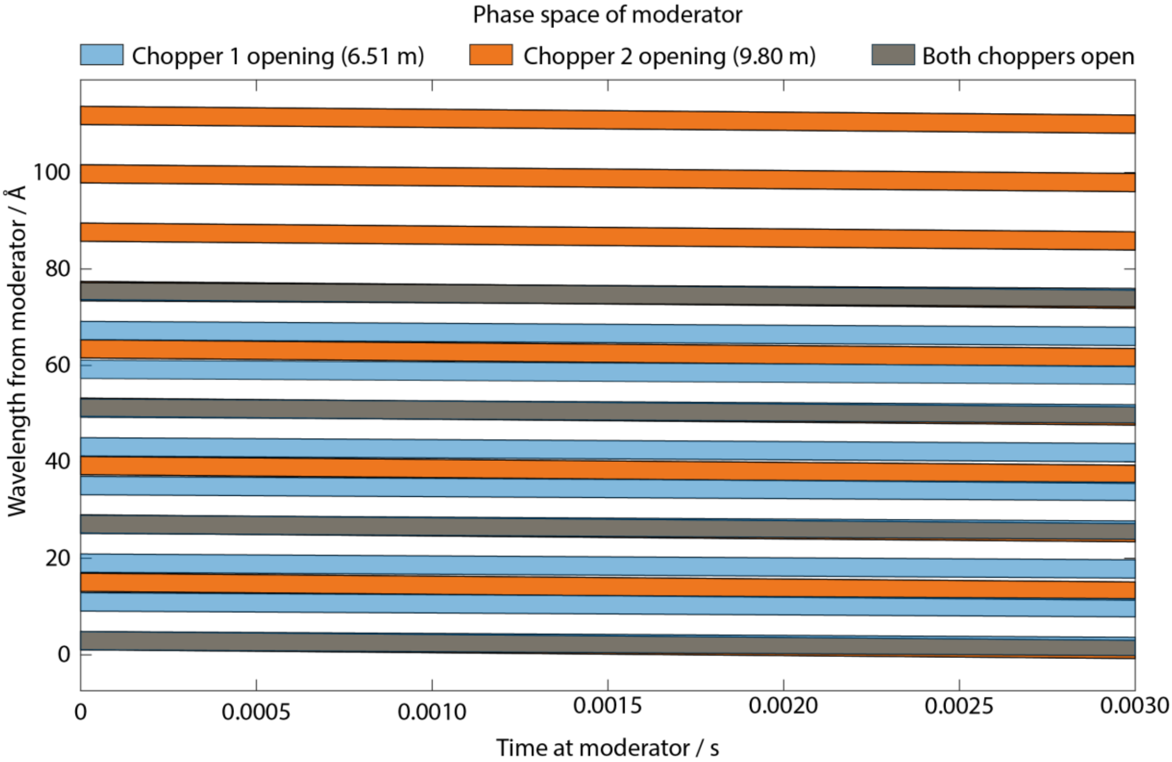

Figure 8.4. Moderator phase space showing neutron wavelengths that pass through the choppers – only the 1-5 Å band is desired. Band spacing is dictated by relative chopper positions, and band width is dependent on the chopper opening size/wavelength range transmitted. Blue bands indicate neutron wavelengths that pass through the first chopper, orange by the second. Grey regions indicate overlaps in chopper openings, indicating the neutron wavelengths that ultimately reach the sample position. The first 10 openings of chopper 1 are shown.

McStas (2.7.1) simulations were performed using a flat-intensity source and a wavelength monitor positioned at 20 m (L_1+L_2). Chopper dimensions were informed by ISIS chopper design engineers, using a disc radius = 0.35 m, disc centre–guide centre = 0.25 m, and a unit width of 0.056 m. Both choppers were set to operate at 50 Hz. In order to transmit the 3.8 Å waveband while in a fully open orientation, chopper apertures of 133.81° and 190.70° were required for positions at 6.51 and 9.8 m, respectively. These calculations were based on a 0.079 × 0.079 m square guide opening.

Due to the finite opening and closing times of the choppers, contaminant neutrons with wavelengths 13 and 17 Å were present – not accounted for by the phase space diagram in Figure 8.4. The position of the second chopper was systematically varied in 0.05 m increments until the 13 Å peak was entirely suppressed. The optimum position was found at 10.05 m where the first (undesired) long-wavelength neutrons were found at ca. 16–18 and 26–29 Å (Figure 8.5). However, their respective intensities, relative to the desired 0–5 Å region are ca. 3 and 4 orders of magnitude lower when using the more realistic flux profile of the hydrogen moderator, as seen by the LOQ port, though diffracted intensity scales with λ^4. These wavelengths can be suppressed with the use of a frame overlap mirror placed in the evacuated beampipe, downstream of the guide.

There is no need to explore moving the first chopper any closer to the moderator from 6.5 m, leaving space for a t_0 chopper as a risk mitigation against gamma radiation. Figure 8.6 shows the distance–time diagram for the optimised chopper positions. Also shown in the Figure are the neutron wavelengths that reach the sample position during the chopper opening and closing times. In order to

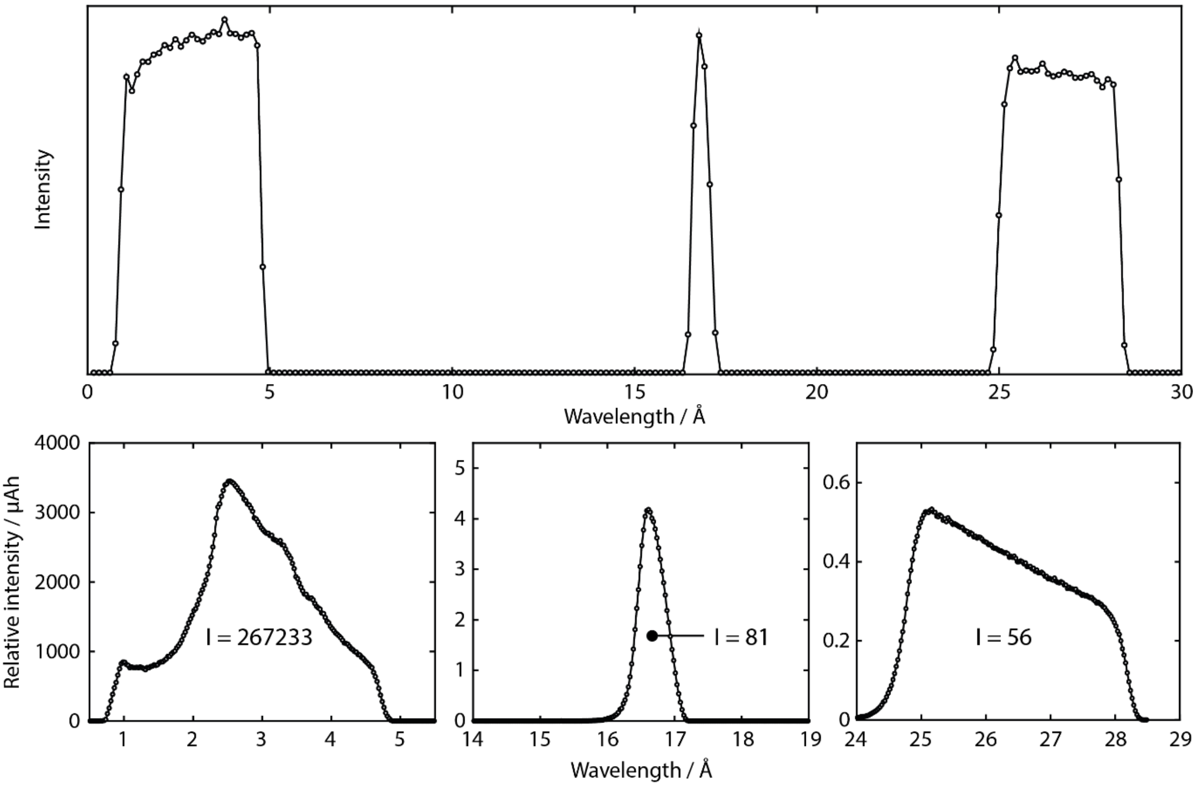

Figure 8.5. Top row: wavelengths reaching detectors at L_1+L_2 = 20 m. Neutron intensities are simulated using a flat intensity, to make clear which longer, spurious, wavelengths are reaching the sample and detectors. Bottom row: wavelength intensity profile simulated using the TS1 hydrogen moderator flux profile. The intensities between each plot are directly comparable, though note the different y-axis scale on each. The integrated, relative, intensities under each peak show that the longer wavelength neutron flux is negligible compared with the principal ca. 1–5 Å neutron band.

minimise these (to the extent shown in the Figure) and reduce overlap with neutrons from the subsequent pulse, double-disc choppers are used at both positions, operating at 50 Hz. Ultimately this leads to a usable waveband of 3.66 Å (0.0185 s).

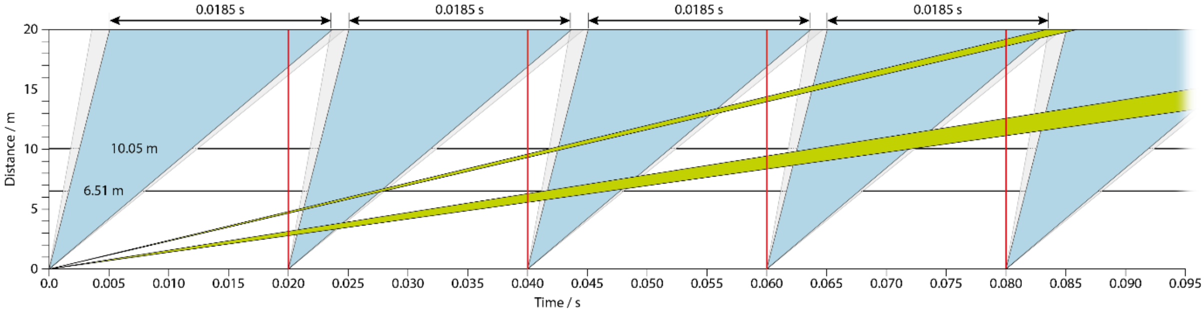

Figure 8.6. Chopper distance/time diagram. Solid black horizontal lines at 6.51, and 10.05 m show the time regime over which the choppers are closed. Vertical red lines indicate the proton pulse frequency on TS1. Blue bands show the neutron time-of-flight transmitted by the choppers when they are fully open. The grey bands indicate additional neutrons that pass through the choppers as they are opening/closing. Ultimately, this leads to a 0.0185 s (3.66 Å) time region that is free of any overlap with other neutrons. Green bands show long-wavelength neutrons reaching the detector (see Figure 8.5).

8.7. Previous (pre-review) design details for guide

7.5 × 0.079 × 0.079 m guide, starting at 6.5 m from moderator and ending 5.5 m from sample.

A key driver is high brilliance transfer across the full wavelength range; made possible by the inclusion of a simple linear guide. The geometry was optimised using McStas simulations. In all cases, the guide entrance was located at 6.5 m (positioned to start immediately after the first chopper), beyond the boundary of the wax shielding on TS1.

The maximum beam divergence that can be used is highly-dependent on the sample unit-cell geometry and crystal mosaicity. Where possible, a large divergence can be used to maximise neutron flux and minimise counting times. Consultation with instrument scientists on MaNDi showed that it was rare for them to use the maximum possible beam divergence (ca. ±0.4°), given the most commonly-encountered sample unit-cell sizes. LMX will target smaller macromolecular unit cells than MaNDi is optimised for, but it will also encounter much smaller unit cells as part of the chemical crystallography programme, and thus be able to take advantage of larger beam divergence. Though background levels scale with divergence, ±0.4° does not cause issues for the MaNDi instrument where good a signal:noise ratio is important. Therefore, the LMX guide was optimised to also transport ±0.4° divergence.

A series of guide dimensions were explored, which allowed the transport of neutrons with divergence up to ±0.4°. Simulations investigating detector pixel sizes/L_2 indicated that ±0.4° is likely a larger divergence than will be used for typical samples, however it offers the ability to transport additional neutrons where allowed by the sample crystal structure. The maximum sample size – 2.5 × 2.5 mm, identified in the Key Drivers – was assumed as this forms the more challenging case for brilliance transfer calculations. In all cases, the (square) guide opening was scaled with the length of the guide to transport a maximum of ±0.4° divergence, illustrated by the schematic in Figure 8.7.

Figure 8.8 shows the brilliance transfer for systematically varying guide length as a function of wavelength. All simulations used an *m*-coating = 5. Over the 1–5 Å waveband, the 7.5 and 10 m guides offer the highest brilliance transfer, though 7.5 m outperforms 10 m at shorter wavelengths. Thus, the optimum case for ±0.4° was found using a guide length of 7.5 m, corresponding to a square opening of 0.079 x 0.079 m. Reducing beam divergence and/or sample size leads to improved brilliance transfer. Subsequently, the *m*-grade of the supermirror coating was explored, shown in Figure 8.8. The natural instrument divergence is also plotted here, i.e. $m = 0$, where brilliance transfer is reduced to ca. 20% for ±0.4°, and ca. 50% for ±0.25°. It is clear that for reduced beam divergence, $m = 3$ is sufficient for near-100% brilliance transfer. The final *m*-grade chosen will need to be tensioned against cost analysis, though $m < 2$ is insufficient for transporting short wavelengths. The total surface area of supermirror coating required is $7.5 \times 0.079 \times 4 = 2.37$ m^2. As the linear guide only transports useful neutrons with a single reflection, the supermirror coating grade will be uniform along the length of the guide to avoid any divergence/wavelength structuring.

The effects of gravity were found to be negligible on brilliance transfer over the 1–5 Å waveband and the 19.5 m incident beam path – the output from simulations demonstrating this are given in the Appendix.

The effects of both guide geometry, and chopper inclusion, are shown in Figure 8.9. The opening/closing time of the choppers leads to the non-uniform divergence at very short, and long wavelengths.

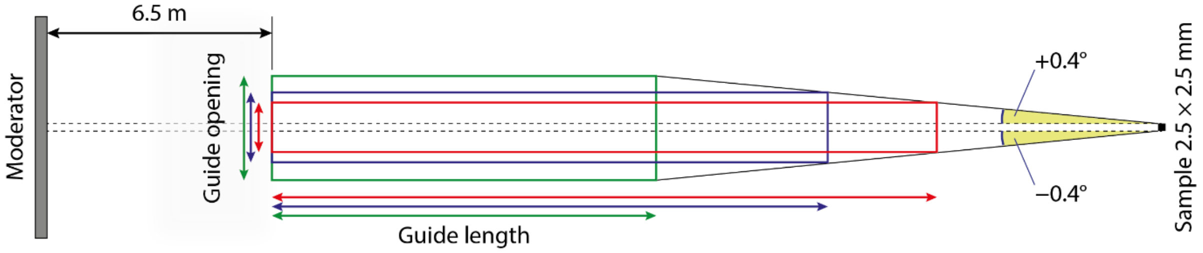

Figure 8.7. Guide dimensions schematic, not drawn to scale. The guide start was held fixed at 6 m from the moderator face, and was scaled to accept ±0.4° divergence from a 2.5 × 2.5 mm sample. The length of the guide (and distance between guide exit-to-sample) scale with the size of the guide opening.

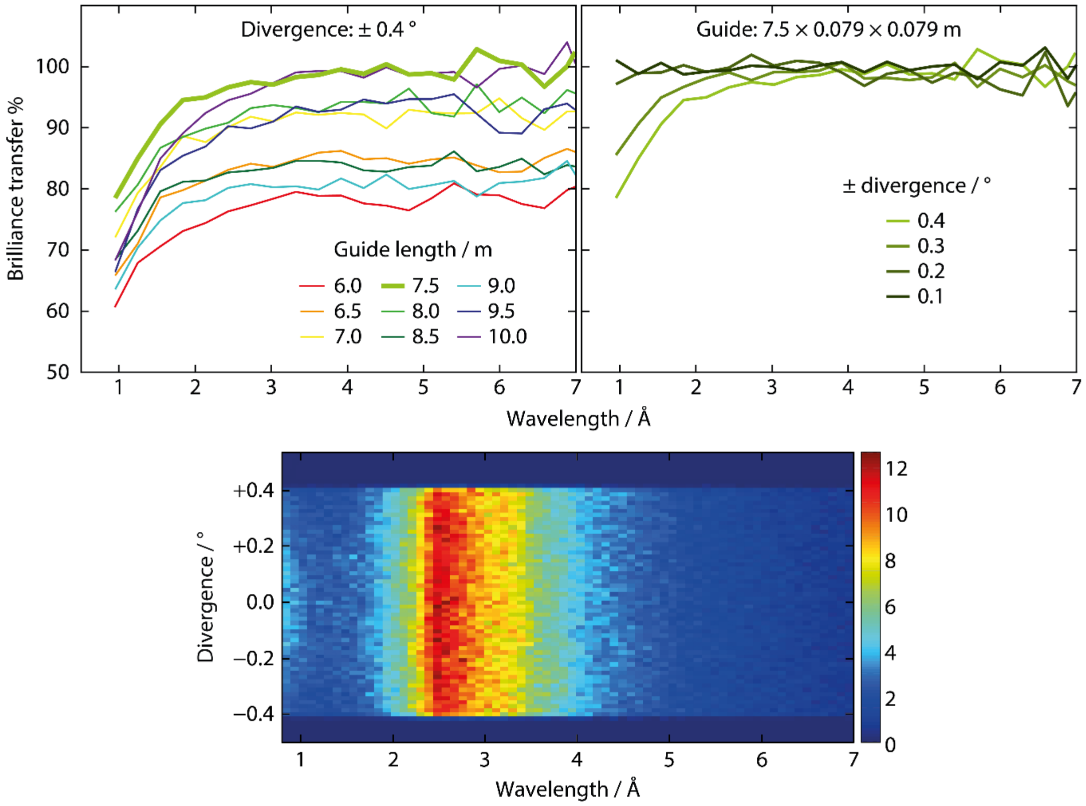

Figure 8.8. Brilliance transfer as a function of guide length for beam divergence ±0.4° and sample size 2.5 × 2.5 mm. The optimum guide length is 7.5 m, shown in bold. These optimised dimensions were used to explore brilliance transfer as a function of beam divergence, showing 100% brilliance transfer across all wavelengths for divergence < ±0.3°. A wavelength/divergence intensity plot shows uniform transport of all divergent neutrons. All simulations use supermirror coating grade $m = 5$.

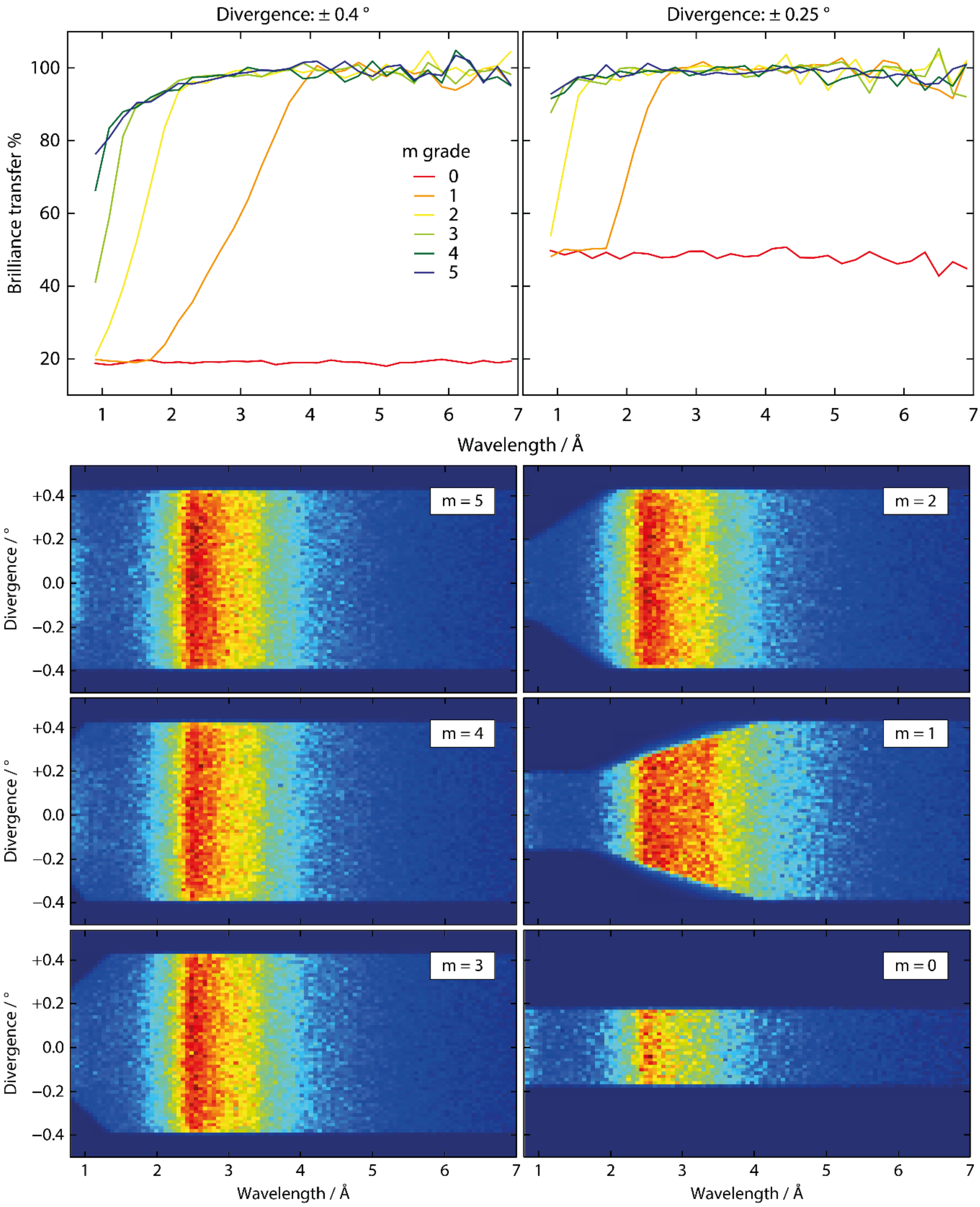

Figure 8.9. Brilliance transfer as a function of m-coating, shown for ±0.4° and ±0.25° beam divergence. Plots with $m = 0$ show the natural instrument divergence. Note that the relative intensities between the wavelength/divergence plots are not directly comparable.

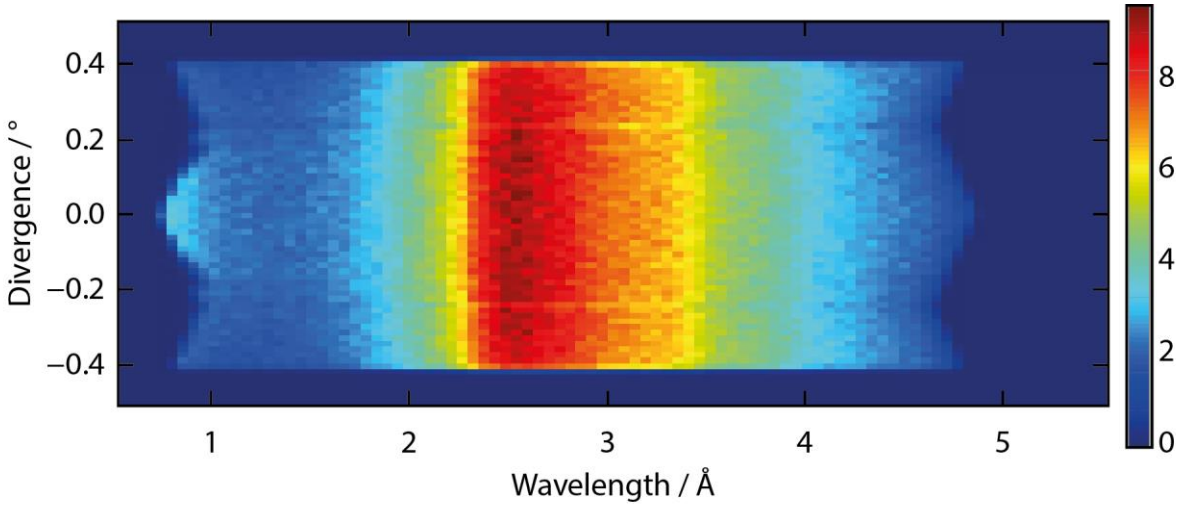

Figure 8.10. The wavelength vs divergence profile at the sample position. The jagged edges arise from chopper opening/closing times. A slight degree of structuring is evident in the divergence profile, particularly at ±0.24°, due to the gaps in the guide for the double-disc choppers.

8.8. McStas simulation files

A McStas file containing the relevant instrument components is supplied separately. The contents of the .instr file are reproduced below:

```
DEFINE INSTRUMENT
LMX(l_min=0.5,l_max=6,L1=19.5,L2=0.5,ModX=0.12,ModZ=0.12,G=9.8,mcoat=5,crystaldim=0.0025,chopwidth=0.035,chop1pos=6.0,chop2pos=9.0,mod2slit=6
.0,mod2guide=7.0,guide2sample=1.5,guidedim=0.035,maxdiv=0.4,coll=0.002,rot=90,pixsize=0.004,detw=0.1,deth=0.768,mos=0.1)

DECLARE
%{
  double emin,emax,L1,ModX,ModZ,tmin,tmax,G,maxdiv,crystaldim,xw,yh,VertDiv,HorDiv;
  double mod2slit,guide1len,guide2len,guidedim,mod2guide,guide2sample,ellipselen,m2gopen;
  double jawstarget,jaws0,jaws1,jaws2;
  double max_hdiv,max_vdiv;
  /* Arrays for storing the calculated brilliance transfer */
  double BT_N[101];
  double BT_p[101];
  double BT_p2[101];
  int neutroncount;
%}

INITIALIZE
%{
  max_hdiv=maxdiv;
  max_vdiv=maxdiv;
  emin=81.799/l_max/l_max;
  emax=81.799/l_min/l_min;

  //guidelen = ((L1-mod2slit)-(mod2guide-mod2slit)-guide2sample);    //Unbroken guide
  guide1len = (chop2pos-(chopwidth/2.0))-mod2guide;
  guide2len = L1-guide2sample-chop2pos-(chopwidth/2.0);

  //Jaws preceding guide - opening
  //first calculate divergence from sample with direct view of moderator
  //Length of the ellipse (almost the same as distance between focal points)
  ellipselen = sqrt(pow(((L1-mod2slit)/2.0),2)+pow((guidedim/2.0),2));
  //guide opening height at entrance
  m2gopen = 2*(sqrt((pow((guidedim/2.0),2)*(1-((pow((ellipselen-(mod2guide-mod2slit)),2))/(pow(ellipselen,2)))))));

  jawstarget = (RAD2DEG*atan((m2gopen/(L1-mod2guide))));
  //now set incident jaws
  jaws0 = ((L1-mod2slit)*(tan(DEG2RAD*jawstarget)))+(crystaldim/2.0);
  //Jaws at end of guide - opening size considers crystal size and desired beam divergence
  jaws1 = ((guide2sample-0.001)*(tan(DEG2RAD*maxdiv)))+(crystaldim/2.0);
  //Jaws at start of sample position - opening size considers crystal size and desired beam divergence
  jaws2 = (L2*(tan(DEG2RAD*maxdiv)))+(crystaldim/2.0);


  //Set xw, yh at slit to match desired beam divergence

  //Use these lines for brilliance transfer calculation
  //xw=(tan(DEG2RAD*maxdiv)*mod2slit)*2.0;
  //yh=(tan(DEG2RAD*maxdiv)*mod2slit)*2.0;

  //Use these lines for illuminating the incident slit only
  xw = jaws0*2;
  yh = jaws0*2;

  printf("\n ellipse length %f\n\n",ellipselen);
  printf("\n guide opening (m): %f\n\n",m2gopen);
  printf("\n mid-ellipse dimension (m): %f\n\n",guidedim);
  printf("\n incident jaws target divergence: %f\n\n",jawstarget);
  printf("\n incident jaws: (m) %f\n\n",jaws0);
  printf("\n post-guide jaws: %f\n\n",jaws1);
  printf("\n pre-sample jaws: %f\n\n",jaws2);
  printf("\n focus square dimension (m): %f\n\n",xw);

%}
//====================================================================================

TRACE

COMPONENT origin = Progress_bar()
AT (0, 0, 0) ABSOLUTE
```

```
// Refurbished TS-1 H2 moderator face
COMPONENT sourceMantid = Commodus_I(
   Face="TS1Mark8_May2017_North05_Loq.mcstas",
   E0 = emin, E1 = emax, modXsize = ModX, modZsize = ModZ,
   xw = xw, yh = yh,
   dist = mod2slit)
AT (0, 0, 0) RELATIVE origin

COMPONENT CalcDiv1 = Arm()
AT (0, 0, 0.001) RELATIVE origin
EXTEND %{
 // Calculate divergence of ray as emitted by the source
 VertDiv =  fabs(RAD2DEG*atan2(vy,vz));
 HorDiv = fabs(RAD2DEG*atan2(vx,vz));
%}

// Measure incoming phase-space for brilliance transfer
COMPONENT BT_in = L_monitor(xwidth=crystaldim, yheight=crystaldim, filename="BT_in.dat",Lmin=l_min, Lmax=l_max, nL=31, restore_neutron=1)
WHEN ((VertDiv <= max_vdiv) && (HorDiv <=  max_hdiv))
AT (0, 0, 0.002) RELATIVE origin

//Incident slit here
COMPONENT slit0 = Slit(
   xmin=-jaws0, xmax= jaws0,
   ymin=-jaws0, ymax= jaws0)
AT (0, 0, mod2slit) RELATIVE origin

// single disc 50 Hz chopper 1
COMPONENT chop1 = DiskChopper(
   theta_0=109.3, radius=0.35, yheight=0.25, nu=50, nslit=1, phase=0, delay=0.004398)
AT (0, 0, (mod2slit+(chopwidth/2.0))) RELATIVE origin

// Elliptical guide - segment 1
COMPONENT guide_seg1 = Elliptic_guide_gravity(
   l=guide1len, xwidth=guidedim, yheight=guidedim,
   linxw=(mod2guide-mod2slit), linyh=(mod2guide-mod2slit),
   loutxw=L1-(chop2pos+(chopwidth/2.0)), loutyh=L1-(chop2pos+(chopwidth/2.0)),
   dimensionsAt="mid",
   m=mcoat, enableGravity=1.0)
AT (0, 0, mod2guide) RELATIVE origin

// single disc 50 Hz chopper 2
COMPONENT chop2 = DiskChopper(
   theta_0=164.2, radius=0.35, yheight=0.25, nu=50, nslit=1, phase=0, delay=0.006598)
AT (0, 0, chop2pos) RELATIVE origin

// Elliptical guide - segment 2
COMPONENT guide_seg2 = Elliptic_guide_gravity(
   l=guide2len, xwidth=guidedim, yheight=guidedim,
   linxw=(chop2pos+(chopwidth/2.0))-mod2slit, linyh=(chop2pos+(chopwidth/2.0))-mod2slit,
   loutxw=guide2sample, loutyh=guide2sample,
   dimensionsAt="mid",
   m=mcoat, enableGravity=1.0)
AT (0, 0, (chop2pos+chopwidth/2.0)) RELATIVE origin

// Slit at guide exit
COMPONENT slit1 = Slit(
   xmin=-jaws1, xmax= jaws1,
   ymin=-jaws1, ymax= jaws1)
AT (0, 0, L1-guide2sample+0.001) RELATIVE origin

// Frame overlap mirror. Theta = k x m x wav. 0.1 x 1 x 29 = 2.9.
COMPONENT mirror = Mirror(
   xwidth=0.7,yheight=0.7,
   m=1.5, center=1, transmit=1)
AT (0, 0, L1-(guide2sample/2.0)) RELATIVE origin
ROTATED ((90-2.0), 0, 0) RELATIVE origin

// Slit at start L2
COMPONENT slit2 = Slit(
   xmin=-jaws2, xmax= jaws2,
   ymin=-jaws2, ymax= jaws2)
AT (0, 0, L1-L2) RELATIVE origin

// Pinhole collimation, 1cm long, 2cm from sample
COMPONENT collimator_in = Slit(
   radius=coll/2)
AT (0, 0, L1-0.03) RELATIVE origin
COMPONENT collimator_out = Slit(
   radius=coll/2)
AT (0, 0, L1-0.02) RELATIVE origin
```

```
// Beam profile at sample position
COMPONENT psd_monitor = PSD_monitor(
   nx=200, ny=200,
   filename="beam_profile.dat",
   xwidth=crystaldim*10.0,
   yheight=crystaldim*10.0,
   restore_neutron=1)
AT (0, 0, L1-0.002) RELATIVE origin

COMPONENT CalcDiv2 = Arm()
 AT (0, 0, L1-0.001) RELATIVE origin
EXTEND %{
   // Calculate divergence of ray after the guide
   VertDiv = fabs(RAD2DEG*atan2(vy,vz));
   HorDiv = fabs(RAD2DEG*atan2(vx,vz));
%}

// Wavelength monitor at sample position
COMPONENT Sample_monitor = L_monitor(
   nL=100, filename="Sample_wav.dat",
   xwidth=crystaldim, yheight=crystaldim,
   Lmin=l_min, Lmax=l_max,
   restore_neutron=1)
AT (0, 0, L1-0.00012) RELATIVE origin

// Measure sample phase-space for brilliance transfer
COMPONENT BT_out = L_monitor(xwidth=crystaldim, yheight=crystaldim, filename="BT_out.dat",Lmin=l_min, Lmax=l_max, nL=31, restore_neutron=1)
WHEN ((VertDiv <= max_vdiv) && (HorDiv <=  max_hdiv))
AT (0, 0, L1-0.0001) RELATIVE origin

// Divergence/wavelength monitor at sample position
COMPONENT sample_divlambda_monitor = DivLambda_monitor(
   maxdiv_h=0.6, nL=101, nh=101,
   xwidth=crystaldim, yheight=crystaldim,
   Lmin=l_min, Lmax=l_max,
   filename="sample_lambda_div.dat",
   restore_neutron=1)
AT (0, 0, L1-0.00001) RELATIVE origin

COMPONENT Sample_arm = Arm()
AT (0, 0, L1) RELATIVE origin

SPLIT 100 COMPONENT Sample = Single_crystal(
   xwidth = crystaldim, yheight = crystaldim, zdepth = crystaldim,
   mosaic = (mos*60)/2.35,  //(60: deg → arcminutes, 2.35: FWHM → Gaussian RMS)
   sigma_inc= -1,
   order = 1,
   reflections="reflections120_0k0_1k0_0k1_1k1_k60.lau")
AT (0, 0, L1) RELATIVE origin
ROTATED (0, -45, 0) RELATIVE Sample_arm
//ROTATED (30, -36, 50) ABSOLUTE  //For .768 det height
EXTEND
%{
 if (!SCATTERED) ABSORB;
%}

COMPONENT Det_arm = Arm()
AT (0, 0, 0) RELATIVE Sample_arm
ROTATED (0, rot, 0) RELATIVE Sample_arm

// PSD Monitor at detector position
COMPONENT Det_psd = PSD_monitor(
   nx=detw/pixsize, ny=deth/pixsize,
   filename="Det_PSD.dat",
   //xwidth=pixsize*npix, yheight=pixsize*npix,
   xwidth=detw, yheight=deth,
   restore_neutron=1)
AT (0, 0, L2) RELATIVE Det_arm

//=========================================================================================

FINALLY
%{
 // This adds another "monitor" that measures BT_out / BT_in
 int j;
 double* tmpN;
 double* tmpp1;
 double* tmpp2;
 double* tmpd1;
 double* tmpd2;
```

```
 tmpN=MC_GETPAR(BT_out,L_N);
 tmpp1=MC_GETPAR(BT_in,L_p);
 tmpp2=MC_GETPAR(BT_out,L_p);
 tmpd1=MC_GETPAR(BT_in,L_p2);
 tmpd2=MC_GETPAR(BT_out,L_p2);
 for (j=0;j<31;j++) {

   BT_N[j]=tmpN[j];
   if (tmpp1[j] != 0) {
     BT_p[j]=tmpp2[j]/tmpp1[j];
   } else {
     BT_p[j]=0;
   }
   if ((tmpp1[j] != 0) && (tmpp2[j] != 0)) {
     BT_p2[j]=sqrt((tmpd1[j]/tmpp1[j])*(tmpd1[j]/tmpp1[j])  + (tmpd2[j]/tmpp2[j])*(tmpd2[j]/tmpp2[j]));
   } else
     BT_p2[j]=0;
 }
// This set of definitions is to avoid getting a '.' in the component name
#ifdef NAME_CURRENT_COMP
#undef NAME_CURRENT_COMP
#define NAME_CURRENT_COMP "BTransfer"
#endif
 DETECTOR_OUT_1D(
                                        "Brilliance transfer",
                                        "Wavelength [AA]",
                                        "BT",
                                        "L", l_min, l_max, 31,
                                        &BT_N[0],&BT_p[0],&BT_p2[0],
                                        "Brilliance_transfer.dat");
%}

END
```